3-D Synthetic Modeling of Anisotropy Effects on SS Precursors: Implications for Mantle Flow in the Transition Zone

Quancheng Huang[1], Nicholas Charles Schmerr[1], Caroline Beghein[2], Lauren Waszek[3], and Ross Maguire[4]

[1]University of Maryland, College Park
[2]University of California Los Angeles
[3]New Mexico State University
[4]University of Maryland

November 21, 2022

Abstract

The Earth's mantle transition zone (MTZ) plays a key role in the thermal and compositional interactions between the upper and lower mantle. Seismic anisotropy provides useful information about mantle deformation and dynamics across the MTZ. However, seismic anisotropy in the MTZ is difficult to obtain from surface wave or shear wave splitting measurements. Here, we investigate the sensitivity to anisotropy of a body wave method, SS precursors, through 3-D synthetic modeling. Our study shows that the SS precursors can distinguish the anisotropy originating from three depths: shallow upper mantle (80-220 km), deep upper mantle above 410-km, and MTZ (410-660 km). Synthetic resolution tests indicate that SS precursors can resolve 3% azimuthal anisotropy where data have an average signal to noise ratio (SNR=7) when azimuthal coverage is sufficient. To investigate regional sensitivity, we apply the stacking and inversion methods to two densely sampled areas: Japan subduction zone and a central Pacific region around the Hawaiian hotspot. We find evidence for a trench-perpendicular fast direction (Θ=87°) of MTZ anisotropy in Japan, but the strength of anisotropy is poorly constrained due to limited azimuthal coverage. We attribute the azimuthal anisotropy to lattice-preferred orientation of wadsleyite induced by trench-parallel mantle flow near the stagnant slab. In the central Pacific study region, there is a non-detection of MTZ anisotropy, although modeling suggests the data coverage should allow us to resolve up to 3% anisotropy. Therefore, the Hawaiian mantle plume does not produce detectable azimuthal anisotropy in the MTZ.

3-D Synthetic Modeling of Anisotropy Effects on SS Precursors: Implications for Mantle Flow in the Transition Zone

Quancheng Huang[1*], Nicholas C. Schmerr[1], Caroline Beghein[2], Lauren Waszek[3,4], Ross R. Maguire[1,5]

1. Department of Geology, University of Maryland, College Park, MD
2. Department of Earth, Planetary, and Space Sciences, University of California, Los Angeles
3. Research School of Earth Sciences, Australian National University, Acton, ACT, Australia
4. Department of Physics, New Mexico State University, Las Cruces
5. Department of Earth and Planetary Sciences, University of New Mexico, Albuquerque, NM

*Corresponding author: Quancheng Huang (Email: qchuang@umd.edu)

Key Points:

- We investigated the sensitivity of SS precursors to azimuthal anisotropy using 3-D synthetics computed from SEPCFEM3D_GLOBE;
- The SS precursors can resolve ≥3% azimuthal anisotropy with average level of noise (signal-to-noise ratio = 7);
- Japan subduction zone is dominated by trench-perpendicular fast direction in the MTZ, whereas the central Pacific anisotropy is undetectable.

Abstract:

The Earth's mantle transition zone (MTZ) plays a key role in the thermal and compositional interactions between the upper and lower mantle. Seismic anisotropy provides useful information about mantle deformation and dynamics across the MTZ. However, seismic anisotropy in the MTZ is difficult to obtain from surface wave or shear wave splitting measurements. Here, we investigate the sensitivity to anisotropy of a body wave method, SS precursors, through 3-D synthetic modeling. Our study shows that the SS precursors can distinguish the anisotropy originating from three depths: shallow upper mantle (80-220 km), deep upper mantle above 410-km, and MTZ (410-660 km). Synthetic resolution tests indicate that SS precursors can resolve $\geq 3\%$ azimuthal anisotropy where data have an average signal to noise ratio (SNR=7) when azimuthal coverage is sufficient. To investigate regional sensitivity, we apply the stacking and inversion methods to two densely sampled areas: Japan subduction zone and a central Pacific region around the Hawaiian hotspot. We find evidence for a trench-perpendicular fast direction (Θ=87°) of MTZ anisotropy in Japan, but the strength of anisotropy is poorly constrained due to limited azimuthal coverage. We attribute the azimuthal anisotropy to lattice-preferred orientation of wadsleyite induced by trench-parallel mantle flow near the stagnant slab. In the central Pacific study region, there is a non-detection of MTZ anisotropy, although modeling suggests the data coverage should allow us to resolve up to 3% anisotropy. Therefore, the Hawaiian mantle plume does not produce detectable azimuthal anisotropy in the MTZ.

Key words: Mantle Transition Zone; Seismic Anisotropy; Subduction Zone; Mantle Flow; Hotspots.

1. Introduction

The Earth's mantle convection is strongly influenced by the properties of the mantle transition zone (MTZ), a distinct layer that controls the thermal and compositional exchange between the upper and lower mantle (e.g., Bercovici & Karato, 2003; Morgan & Shearer, 1993). The boundary of the MTZ is defined by two sharp seismic discontinuities at 410-km and 660-km depths. The formation of these discontinuities is a consequence of the pressure-induced phase changes of upper mantle mineral olivine, and to a lesser extent the garnet phase transitions. Mineral physics experiments show that the phase change of olivine to wadsleyite occurs at 410 km depth, and the dissociation of ringwoodite to bridgmanite + ferropericlase occurs at 660 km depth (Ita & Stixrude, 1992; Ringwood, 1975). The opposite Clapeyron slopes of the olivine phase changes (Ito & Takahashi, 1989; Katsura & Ito, 1989) make them useful for studying the mantle thermal and compositional heterogeneities (Bina & Helffrich, 1994; Helffrich, 2000; Stixrude, 1997) via mapping of MTZ topography (e.g., Flanagan & Shearer 1998).

The SS precursors are seismic body waves that manifest as shear wave reflections occurring at the underside of the 410-km and 660-km discontinuities (Figure 1). The SS precursors have served as a primary tool to investigate topography on these discontinuities at both regional (e.g., Schmerr et al., 2010; Thomas & Billen 2009; Yu et al., 2017) and global scales (e.g., Deuss & Woodhouse, 2002; Flanagan & Shearer, 1998; Gu & Dziewonski, 2002; Houser et al, 2008; Huang et al., 2019; Lawrence & Shearer, 2008). The SS precursors that reflect from the 410-km and 660-km discontinuities are named as S410S and S660S respectively, or generally referred as SdS where d is the depth of discontinuity within the Earth. Several studies of the SS precursors have detected seismic anisotropy in the upper mantle and MTZ (Huang et al., 2019; Rychert et al., 2012, 2014). Seismic anisotropy, the dependence of seismic velocity on direction and polarization, is a useful tool to constrain mantle deformation and dynamics, and it is primarily produced by two key mechanisms: the lattice-preferred orientation (LPO) of intrinsically anisotropic minerals under a dislocation creep regime, or the shape-preferred orientation (SPO) of isotropic materials with distinct elastic properties (e.g., due to compositional layering or lenses of melt). Here we further evaluate the sensitivity of the SS precursors to mantle anisotropy, to demonstrate how these seismic phases can provide insights into mantle deformation and dynamics in the MTZ.

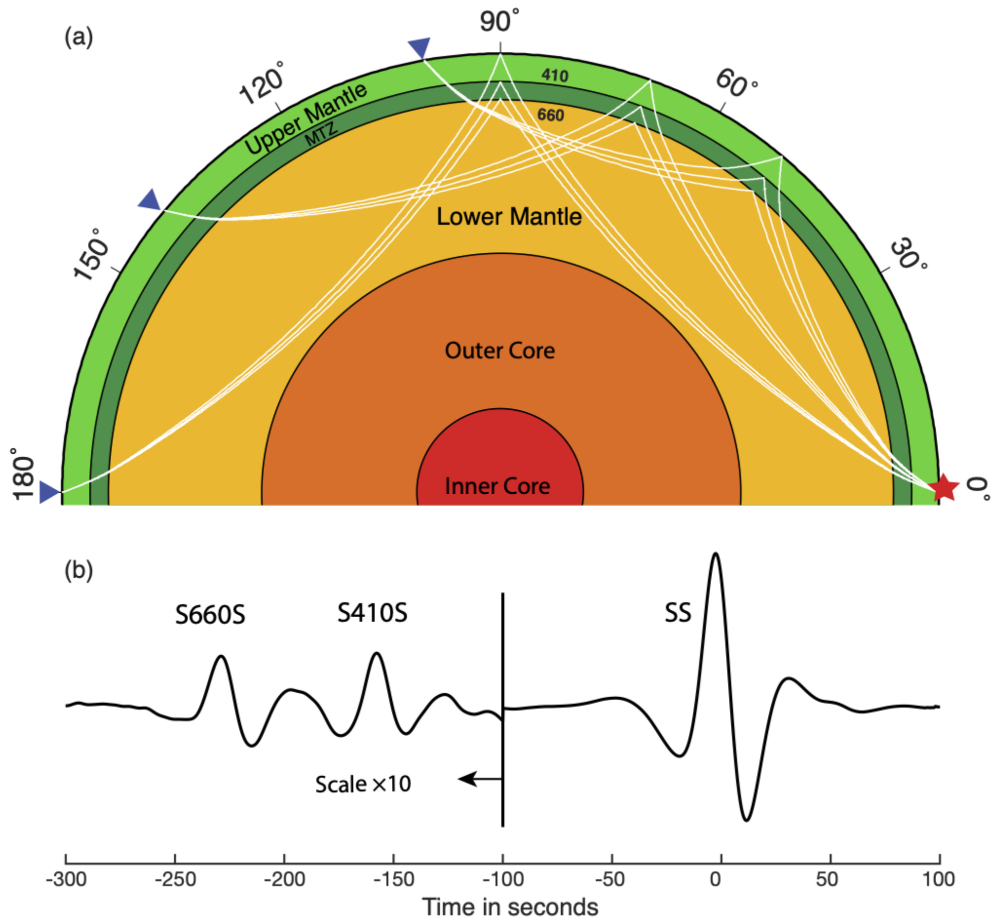

Figure 1. (a) The ray paths of SS phase and SS precursors at the epicentral distances of 100, 140 and 180 degrees. The red star and blue triangles represent the source and receivers respectively. (b) An example of stacked waveform of SS phase and SS precursors. The amplitudes of S410S and S660S are amplified by 10 times to facilitate comparisons with the SS phase.

Observations of upper mantle anisotropy are traditionally obtained from shear wave splitting (e.g., Long & van der Hilst, 2005; Marone & Romanowicz, 2007; Silver & Chan, 1988), surface wave dispersion (e.g., Anderson, 1962; Montagner & Nataf, 1986; Nettles & Dziewonski, 2008) and global tomography models (e.g., Chang et al., 2015; French & Romanowicz, 2014; Moulik & Ekström, 2014). Upper mantle anisotropy is typically interpreted as the LPO of olivine (e.g., Karato et al., 2008) caused by the current pattern of mantle flow in the asthenosphere or the preservation of paleo-flow directions in the lithosphere (i.e., “fossil anisotropy”). At MTZ depths, evidence for seismic anisotropy is more limited, but consistently reported from multiple methods: shear wave splitting (Chen & Brudzinski, 2003; Foley & Long, 2011; Fouch & Fischer, 1996; Tong et al., 1994), surface wave measurements (Debayle et al., 2016; Trampert & van Heijst, 2002; Yuan and Beghein 2013, 2014, 2018), coupling of normal models (Beghein et al., 2008), and inversion of deep earthquake focal mechanisms (Li et al., 2018). The surface wave models that incorporate higher mode surface waves (Debayle et al., 2016; Schaeffer et al., 2016; Yuan and Beghein, 2013, 2014) suggest that ~1% azimuthal anisotropy exists in the MTZ globally, despite regional discrepancies amongst these models. Recently, Ferreira et al. (2019) discovered ubiquitous radial anisotropy in the MTZ and uppermost lower mantle in the vicinity of western Pacific subduction zones. Our previous study using SS precursors (Huang et al., 2019) also found regional evidence for 3% azimuthal anisotropy in the MTZ beneath subduction zones but detected negligible anisotropy (< 1%) at a global scale.

Unlike the upper mantle, where deformation is expressed in the LPO of the mineral olivine, the MTZ may have several mechanisms for accommodating seismic anisotropy. For example, the MTZ anisotropy in subduction zones has primarily been attributed to the LPO of wadsleyite (Kawazoe et al., 2013), although the SPO of subducting slabs has also been proposed (Faccenda et al., 2019). In the upper transition zone (410-520 km), wadsleyite has up to ~14% single-crystal Vs anisotropy (Sawamoto et al., 1984; Sinogeikin et al., 1998; Zha et al., 1997), making wadsleyite the main candidate mineral for accommodating anisotropy at these depths. Below 520 km, ringwoodite is nearly isotropic with a cubic structure (Kiefer et al., 1997; Li et al., 2006; Sinogeikin et al., 2003; Weidner et al., 1984). Other minerals such as majorite garnet and clinopyroxene have either weak single-crystal anisotropy, or not enough mineral fraction abundance to accommodate the seismic observations of MTZ anisotropy (Bass and Kanzaki, 1990; Pamato et al., 2016; Sang and Bass, 2014). Slab mineralogy and layering may provide an alternative mechanism for accommodating anisotropy in the deep transition zone (Faccenda et al., 2019). Although wadsleyite can accommodate up to 14% anisotropy, it must be aligned by mantle dynamics into a fabric detectable by seismic waves. Numerical simulations of strain-induced fabric of mantle mineral aggregates are therefore key to understanding the relationship between mantle flow direction (or strength) and fast direction (or strength) of seismic anisotropy in the MTZ. Previous modeling has primarily focused on the upper mantle anisotropy (e.g., Becker et al., 2006), whereas few studies explore deeper anisotropy in the MTZ and uppermost lower mantle (Faccenda, 2014; Sturgeon et al., 2019). For example, Sturgeon et al. (2019) predicts that up to ~2% Vs radial anisotropy may form in the MTZ beneath subduction zones. Mineral physics modeling by Tommasi et al. (2004) predicts that ~1% Vs azimuthal anisotropy can exist within the MTZ.

Although the sensitivities of SS precursors to the topography of 410-km and 660-km discontinuities have been investigated (Bai et al., 2012; Koroni & Trampert, 2016; Zhao & Chevrot, 2003), their sensitivity to azimuthal anisotropy at MTZ depths remains unexplored. Motivated by both geodynamic and mineral physics predictions, we use SS precursors to better constrain anisotropy at MTZ depths, thereby illuminating the dynamics of the upper mantle. In this study, we construct 3-D models of anisotropy and propagate synthetic seismic waves through the model to test the sensitivity of SS precursors to azimuthal anisotropy. We next compare the results of our modeling to observations in the central Pacific region and Japan subduction zone to determine the detectability and sensitivity of the SS precursory phases to MTZ anisotropy. Finally, we interpret the mantle flow pattern in the MTZ in the context of our observations.

2. Methods

2.1 SS Dataset

We expanded a global hand-picked SS dataset described in Huang et al. (2019) and Waszek et al. (2018) to include earthquakes in the depth range 0-75 km (previously only 0-30 km) and broadband stations from 1988 to 2017. Any records with signal-to-noise ratio (SNR), which was computed from the amplitude of SS phase over the maximum amplitude in a noise window (65 to 275 seconds before SS phase), lower than 2.5 were removed from the dataset. The final SS dataset consists of 58,566 seismograms, which is ~10,000 more than the previous dataset. We used the transverse component of the data to study the azimuthal anisotropy. To remove seismic noise, we filtered the data between 15 and 50 s using a Butterworth band-pass filter and aligned the waveform at the peak amplitude of SS phase. Each SS seismogram was normalized to unity to equalize the SS arrivals across events and stations.

2.2 3-D Synthetics

We used the spectral element code SPECFEM3D_GLOBE (Komatitsch & Tromp, 2002 a, b) to compute 3-D synthetic SS precursor waveforms. The mesh consisted of 6 domains with 320 spectral elements on each side. Therefore, the minimum period of the synthetics was 13.6 seconds. We created 13 earthquakes around the target region to provide ideal azimuthal coverage (Figure 2 & 3). The focal mechanism of each earthquake was set to maximize the SH energy in the receiver direction. We chose a dense array to guarantee ideal azimuthal coverage as well. After computing the synthetics, we generated random noise based on the realistic power spectrum of Earth's noise (Peterson 1993) and added it to the synthetics. The synthetics were then processed in the same way as the data in section 2.1.

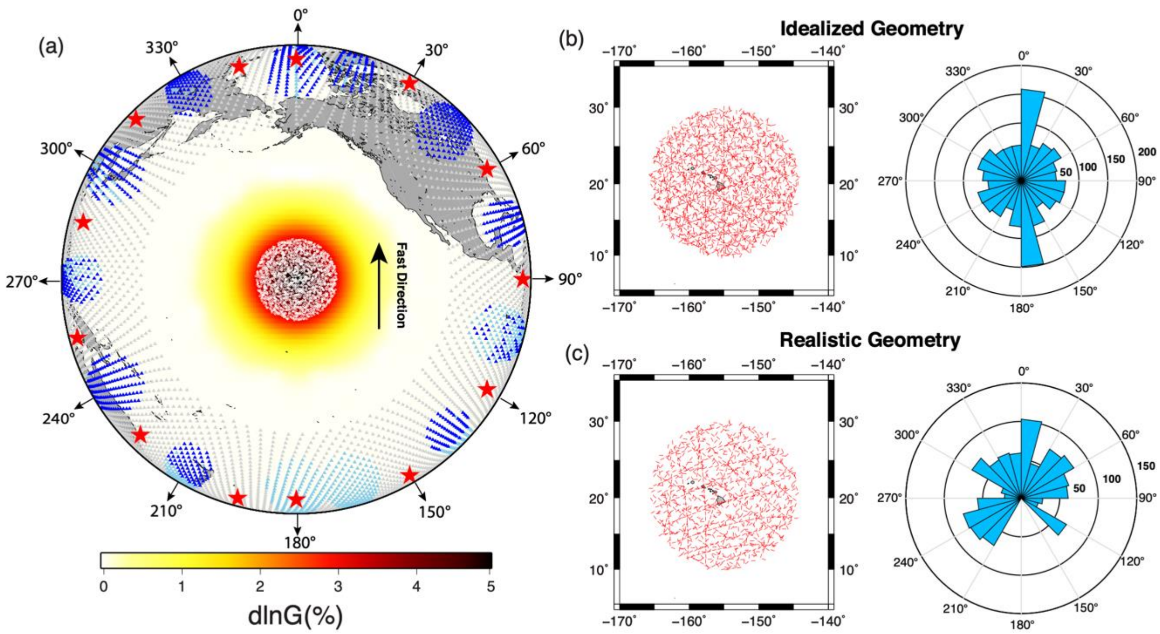

Figure 2. (a) The source-receiver geometry for the model in the central Pacific region. The red stars denote the earthquake sources. The input fast direction is due north (0°). The triangles represent all the stations: the light blue + dark blue stations are the ones used for the idealized geometry; the dark blue stations only are the ones used for the realistic geometry; the grey stations are the unused ones. The white points in the center are the SS bounce points with a bin radius of 10 degrees (~1100 km). (b) The SS bounce points in the idealized geometry (left) and their azimuthal distribution (right). (c) The SS bounce points in the realistic geometry (left) and the azimuthal distribution of the bounce points (right) which mimics the azimuthal coverage of data in this region.

We chose two study regions that are densely sampled by the SS phase: (1) the central Pacific region near Hawaii (Figure 2) and (2) Japan subduction zone (Figure 3). The goal was to simulate the azimuthal anisotropy generated by a mantle plume versus a subducting slab. In each region, we created two types of source-receiver geometries: idealized, and realistic geometry. The idealized geometry provided at least 100 records in each 15° azimuthal bin to ensure enough data for the stacking of SS precursors. The realistic geometry was a subset of the idealized geometry to mimic the actual azimuthal coverage of the data that sample each region. This anisotropic structure was overprinted on the Preliminary Reference Earth Model (PREM, Dziewonski & Anderson, 1981) at three depth ranges: (1) the shallow upper mantle (80 – 220 km); (2) the deep upper mantle (250 – 400 km); (3) the MTZ (400 – 670 km). The boundaries of these layers coincide with the discontinuities in PREM such as 220-, 400- and 670-km discontinuities. The models at each depth included three strengths of anisotropy: 1%, 3% and 5%. The input fast directions were due north (0°) in the central Pacific bin and trench perpendicular (270°) in the Japan bin. We set the radius of the central Pacific bin to 10 degrees (~1100 km) and the size of Japan bin was 1500 × 1000 km. The choice in size of the central Pacific structure was controlled by the standard deviation of normal distribution, and we explored the effects of lateral size of anisotropic structures on resolution using 5- and 2.5-degrees radius.

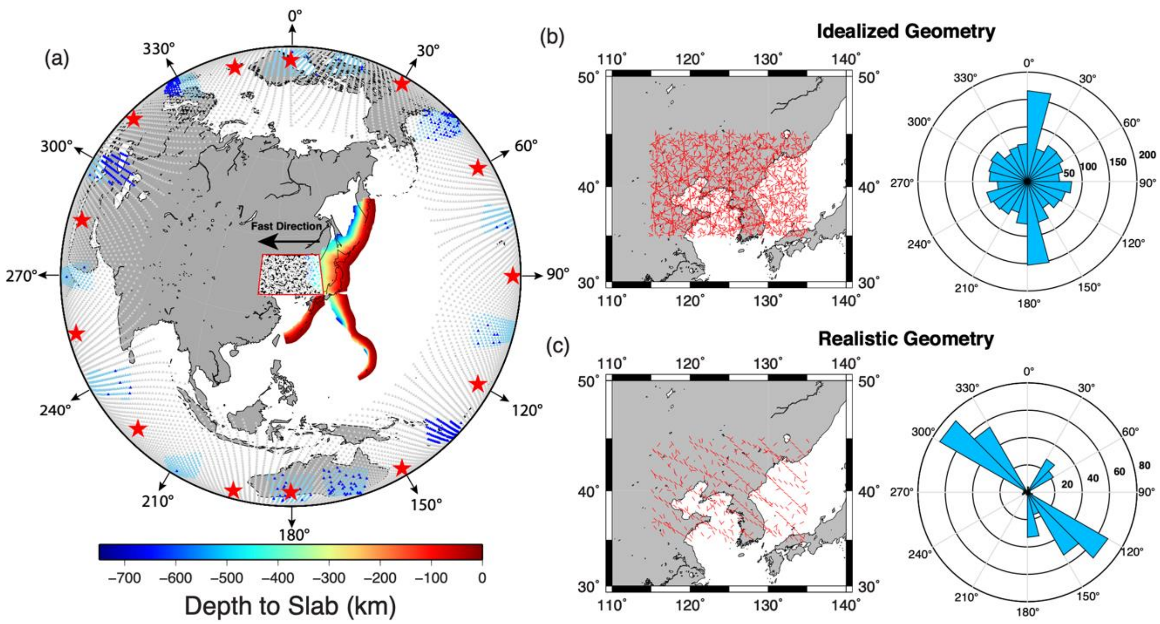

Figure 3. (a) The source-receiver geometry for the model in Japan subduction zone. The source, receiver and bounce point legends are the same as Figure 2. The study region is highlighted by the red box and the size is 1500 km×1000 km. The strength of anisotropy is a uniform value thus represented in black color and the fast direction is trench-perpendicular (270°). The values of slab depths are from Slab 1.0 model (Hayes et al., 2012). (b) The SS bounce points in the idealized geometry (left) and their azimuthal distribution (right). (c) The SS bounce points in the realistic geometry (left) and their azimuthal distribution (right).

2.3 Stacking and Corrections

SS precursors are typically similar in amplitude to background noise or less, thus their retrieval requires stacking when noise is present. Here, we followed the stacking methods of Schmerr and Garnero (2006) to stack the precursors along the predicted travel-time curves from PREM. We chose 125 degrees as our reference distance and applied distance exclusion windows (0°-100° and 135°-145° for S410S; 0°-115° and 165°-180° for S660S) to avoid interferences of other seismic phases. We stacked the data by azimuth of the ray-path at the central bounce-point of SS to study the azimuthal variations of SS precursor travel-times and amplitudes. The 2σ uncertainties of travel-time and amplitude measurements were estimated from a bootstrapping technique that implemented 300 resamples, allowing replacements within each bin (Efron & Tibshirani, 1986).

We applied a series of travel-time and amplitude corrections to ensure that precursor travel-times and amplitudes were not contaminated by factors other than anisotropy, and then inverted for azimuthal anisotropy. Full details regarding travel-time and amplitude correction methods are contained in Huang et al. (2019). (1) The travel-times of SS precursors are affected by the lateral heterogeneities of crustal and upper mantle structures. We used CRUST 2.0 model (Bassin et al., 2000) for the crustal corrections and S40RTS model (Ritsema et al., 2011) for the tomography corrections. We computed travel-time residuals with respect to PREM based on 1-D ray tracing as pre-stacking travel-time corrections for each individual record. (2) We also corrected for the travel-time perturbations caused by topography of 410-km and 660-km discontinuities using the MTZ topography measurements by Huang et al. (2019). We computed the topography corrections from the differences between the local 410-km, 660-km depths and their global mean depths. (3) The amplitudes of SS precursors were corrected for attenuation, geometrical spreading, and focusing and defocusing effect using the 1-D synthetics generated by GEMINI code (Friederich and Dalkolmo, 1995). We calculated the amplitude ratios between the stacking results of data and corresponding 1-D synthetics and multiplied by the amplitudes at reference distance (125°) to remove these effects on amplitudes. The observed data were corrected for both travel-time and amplitude, but the 3-D SPECFEM synthetics were only corrected for amplitude since no 3-D velocity structures existed in PREM.

2.4 Inversion for Azimuthal Anisotropy

After applying the amplitude and travel time corrections, we inverted for the strength and fast direction of azimuthal anisotropy from SdS travel-times and amplitudes. In a transversely isotropic medium with a horizontal symmetry axis, the velocity of vertically propagating SH wave is expressed as the following equations (Crampin, 1984; Montagner and Nataf, 1986):

$$\rho V_{qSH}^2 = L - G_c cos2\psi - G_s sin2\psi \tag{1}$$

$$L = \rho V_{SV}^2 = \frac{1}{2}(C_{44} + C_{55}) \tag{2}$$

where ρ is density, V_{qSH} is the velocity of quasi-SH wave, ψ is the azimuth of wave propagation direction, L is a function of the isotropic SV wave velocity and can be expressed as elastic parameters C_{ij} , $Gc = \frac{1}{2}(C_{55} - C_{44})$ and $Gs = C_{54}$ are the 2ψ azimuthal terms of L (Montagner et al., 2000). The strength of anisotropy (G) and fast direction (Θ) are derived from the G_c and G_s parameters:

$$G = \sqrt{G_s^2 + G_c^2} \tag{3}$$

$$\Theta = \frac{1}{2} arctan\left(\frac{G_s}{G_c}\right) \tag{4}$$

First, we built simple 1-D anisotropy models with constant G_c and G_s values at the three depth ranges mentioned in section 2.2. Then, we computed the predicted travel-times and amplitudes based on equation (1) and (2). Finally, we used a grid-search method to find the best-fitting G_c and G_s values and used equation (3) and (4) to compute the best-fitting fast direction and strength of anisotropy. The uncertainties of the anisotropy fit are estimated from the chi-squared statistics using p-values for 2 standard deviations.

3. Results

We first investigated the effect of depth, strength, and size of anisotropy on measurement resolution using clean synthetics in the central Pacific region. Next, we examined the data in the central Pacific region and Japan subduction zone from which we inverted azimuthal anisotropy and quantified the uncertainties. Finally, we added realistic noise to the 3-D synthetics for direct comparison to the data, and we also explored the effect of source-receiver geometry on the resolution.

3.1 The Effects of Depth, Strength and Size of Anisotropy

Unlike shear wave splitting measurements, SS precursors can distinguish the depths of anisotropy structures based on the combinations of five differential travel-time and amplitude ratio measurements: S410S-SS time, S660S-SS time, S660S-S410S time, S410S/SS and S660S/SS amplitudes. In order to understand the effect of depth, we fixed the size of anisotropy to be 10-degrees in radius and varied the depths of anisotropy in the model and performed the following synthetic tests.

Test (1): Shallow Upper Mantle, Fixed Size. The first experiment simulates anisotropy in the asthenosphere (80-220 km), which is often attributed to the LPO of olivine (Figure 4a). The SS travel-times are sensitive to the asthenosphere anisotropy and their variations are mapped to S410S-SS (Figure 4b) and S660S-SS travel-times (Figure 4c) since SS is our reference phase. The S660S-S410S time (Figure 4d) and amplitudes (Figure 4e) remain constant because their ray paths do not encounter the anisotropic layer.

Test (2): Deep Upper Mantle, Fixed Size. The second case creates the scenario where anisotropy is present in the deep upper mantle (250-400 km, Figure 5a), which can still be caused by the fabric of olivine (e.g., Mondal and Long, 2020). In this model, the S410S/SS amplitude starts to vary with azimuth due to the change of reflection coefficients at 410-km (Figure 5e), whereas the S660S-S410S time (Figure 5d) and S660S/SS amplitudes (Figure 5e) remain constant.

Test (3): MTZ anisotropy, Fixed Size. The final scenario models an anisotropic layer in the MTZ where the LPO of wadsleyite and ringwoodite are formed (Figure 6a). The

S660S-S410S time becomes an independent measurement for MTZ anisotropy (Figure 6d) which is not affected by the upper mantle anisotropy. This model includes anisotropy throughout the whole MTZ so both S410S/SS and S660S/SS amplitudes (Figure 6e) display variations with azimuth. These two amplitudes have opposite trends because the MTZ anisotropy is below the 410-km but above the 660-km discontinuity, therefore changing the signs of reflection coefficients.

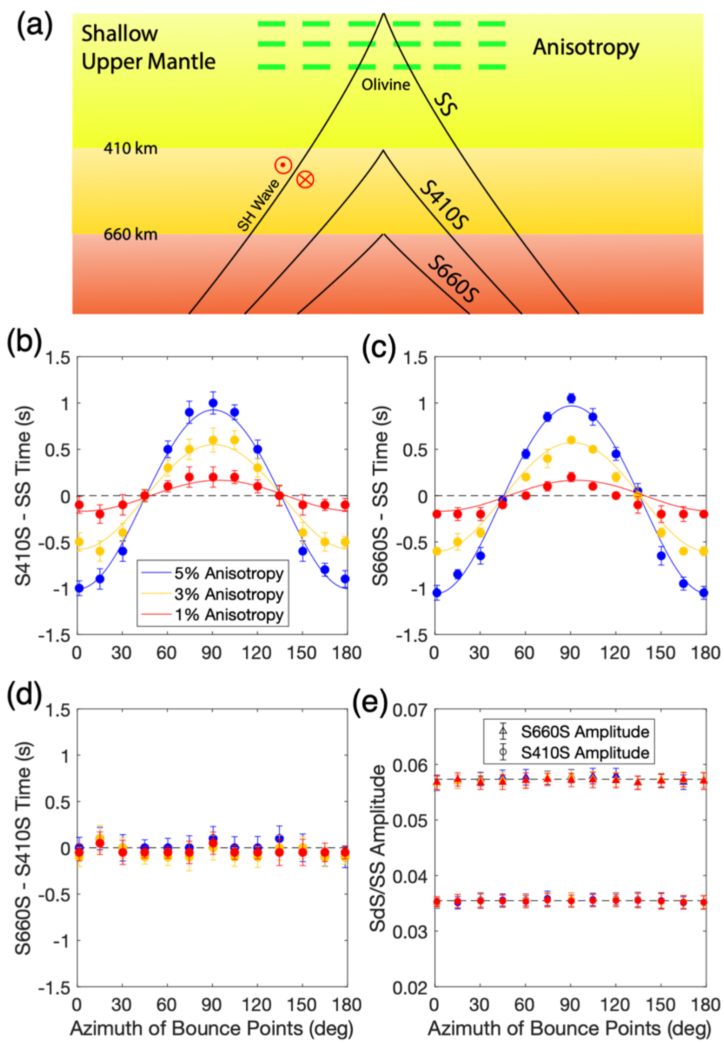

Figure 4. (a) The anisotropy model in the shallow upper mantle (80-220 km). The green bars represent the LPO of olivine. The black curves are the ray paths of SS precursors beneath the bounce point region. The measurements of (b) S410S – SS time, (c) S660S – SS time, (d) S660S – S410S time, (e) S410S/SS and S660S/SS amplitudes from the azimuthal stacking of SPECFEM3D synthetics as a function of bounce point azimuths. The solid lines are the best-fitting models for 1%, 3% and 5% input anisotropy. The dashed lines denote the mean values of each measurement.

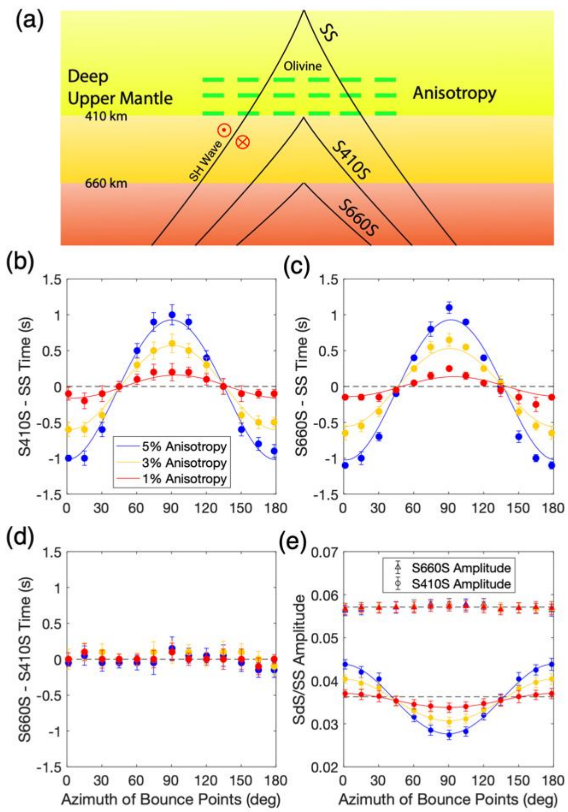

Figure 5. (a) The same as Figure 4 but for anisotropy model in the deep upper mantle (250 – 400 km). The measurements of (b) S410S – SS time, (c) S660S – SS time, (d) S660S – S410S time, (e) S410S/SS and S660S/SS amplitudes from the azimuthal stacking of SPECFEM3D synthetics as a function of bounce point azimuths.

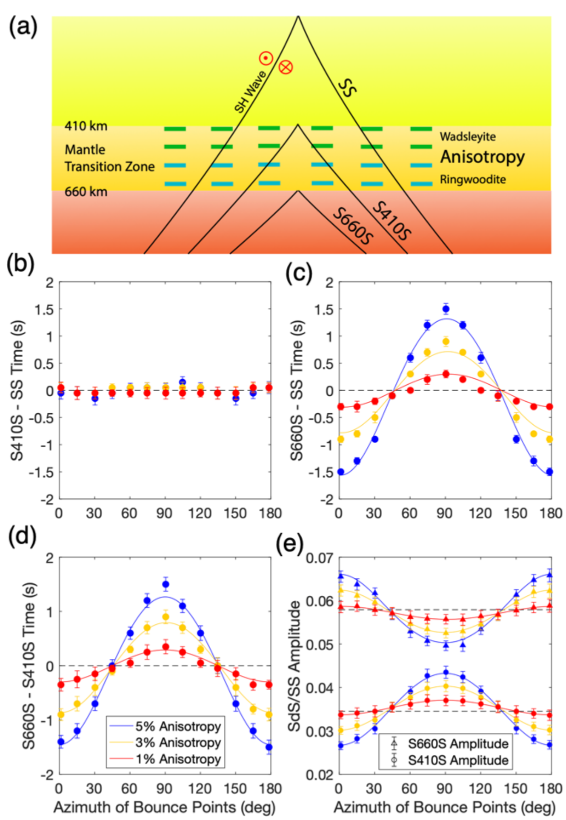

Figure 6. (a) The same as Figure 4 but for anisotropy model in the MTZ (400 – 670 km). The green and blue bars represent the LPO of wadsleyite and ringwoodite respectively. The measurements of (b) S410S – SS time, (c) S660S – SS time, (d) S660S – S410S time, (e) S410S/SS and S660S/SS amplitudes from the azimuthal stacking of SPECFEM3D synthetics as a function of bounce point azimuths.

Test (4): Fixed Depth in the MTZ, Varied Size: The strength and size of anisotropy control the peak-to-peak amplitudes of SdS travel-time and amplitude variations. In this test, the bin radius was fixed at 10 degrees and the anisotropy layer is in the MTZ. Then, we varied the strength and size of anisotropy and identified four measurements that were sensitive to MTZ anisotropy: S660S-SS time (Figure 7a), S660S-S410S time (Figure 7b), S410S/SS and S660S/SS amplitude (Figure 7c).

The first column of Figure 7 shows that 3-5% MTZ anisotropy with 10-degree radius can translate into 0.9-1.5 seconds travel-time variations respectively. Generally, the variations caused by anisotropy need to be greater than the corresponding uncertainties of SdS travel-times or amplitudes to become detectable. The amplitudes of uncertainties are directly related to the noise level in the data or synthetics. We estimated the average 2σ uncertainties by adding random noise (SNR=7, average noise level of our SS dataset) to synthetics before stacking (see section 2.2). The average uncertainties, which are shown as gray shaded regions in Figure 7, can be used as detection thresholds for SdS travel-times and amplitudes. When the radius is 10 degrees, Figure 7 illustrates that the S660S-SS and S660S-S410S times can both detect $\geq$3% anisotropy. The uncertainties of SdS amplitudes are generally larger in terms of percentage so anisotropy is more difficult to detect, requiring over 5% anisotropy to be detectable. Moving from left to right in Figure 7, the peak-to-peak amplitudes of SdS travel-times and amplitudes both decrease as the size of the structure is reduced. When the radius is decreased to 5 degrees, the S660S-SS and S660S-S410S times can only detect $\geq$5% anisotropy, whereas the variations of SdS amplitudes are below the detection thresholds. The 2.5-degrees radius structures are too small to be detectable because all the variations become much lower than the detection thresholds.

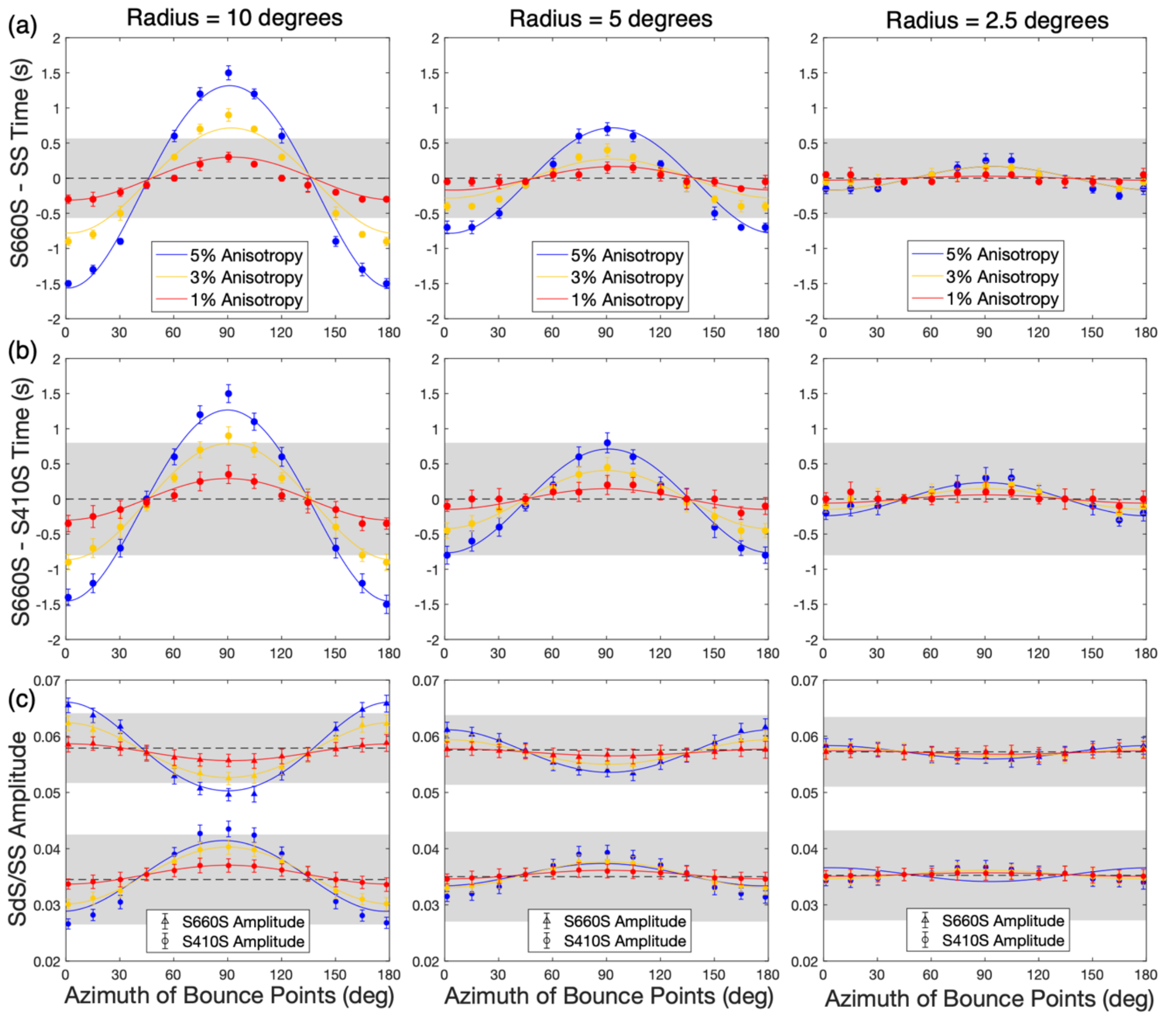

Figure 7. The effect of anisotropy size and strength on SS precursors. The measurements of (a) S660S – SS time, (b) S660S – S410S time, (c) S410S/SS and S660S/SS amplitudes as a function of bounce point azimuths. The radius of anisotropy decreases from 10 degrees to 5 degrees and 2.5 degrees from left to right, whereas the bin radius remains 10 degrees. The depth of anisotropy is in the MTZ (400 – 670 km). The solid lines represent the best-fitting models for 1%, 3% and 5% input anisotropy. The dashed lines denote the mean values of each measurement. The gray shaded regions represent the detection thresholds for SdS travel-times and amplitudes estimated from the stacking of synthetics with average noise level (SNR=7).

3.2 Central Pacific Data and Resolution Test

Following the depth, strength, and size 3-D synthetic tests, we used our modeling to study the detectability and resolution of anisotropy for an SS precursor dataset sampling the central Pacific region. In Figure 8a, the MTZ thickness beneath the central Pacific bin is thinner than average predominantly due to the hot thermal anomalies caused by the

Hawaiian hot spot (e.g., Schmerr et al., 2010). This bin has sufficient azimuthal coverage and number of records (NR > 100) in five azimuthal bins (Figure 8c), therefore both S410S and S660S were observed in data and synthetics from azimuthal stacking (Figure 8b). We measured the S660S-S410S times from the azimuthally stacked data results and inverted for azimuthal anisotropy after removing topography variations. As shown in Figure 8d, the recovered strength of anisotropy (dlnG=2.9±2.8%) is not significantly above zero based on the chi-squared statistics, which suggests that the central Pacific region has very weak MTZ anisotropy.

To further test the weak anisotropy hypothesis, we added noise to the 3-D synthetics (see Section 2.2) with different SNR values, using both idealized and realistic geometries to explore the effect of data coverage in the central Pacific region (Figure 2). The goal was to test the resolution of the SS precursors in the central Pacific region and determine the minimum strength of anisotropy that would provide a detectable signal in the data. To quantify detectability of anisotropy, we define a parameter ε as the total misfit of the best-fitting model compared to the input anisotropy model:

$$\varepsilon_G = \sqrt{\left(\frac{dlnG_{out} - dlnG_{in}}{dlnG_{in}}\right)^2 + \left(\frac{2\sigma_G}{dlnG_{out}}\right)^2} \tag{5}$$

$$\varepsilon_\Theta = \sqrt{\left(\frac{\Theta_{out} - \Theta_{in}}{\pi/2}\right)^2 + \left(\frac{2\sigma_\Theta}{\pi/2}\right)^2} \tag{6}$$

where ε_G and ε_Θ are the total misfit for strength of anisotropy and fast direction respectively, $dlnG_{in}$ and Θ_{in} are the input strength of anisotropy and input fast direction respectively, $dlnG_{out}$ and σ_G are the best-fitting strength of anisotropy and 1σ error from inversions respectively, Θ_{out} and σ_Θ are the best-fitting fast direction and 1σ error respectively. ε can quantify the resolution as it takes into account the misfit between the input and best-fitting anisotropy parameters, and the uncertainties of the best-fitting model as well. ε is a positive value, and if $\varepsilon < 1$, we define this scenario as a detectable case. Conversely, if $\varepsilon \geq 1$, we define this scenario as a non-detectable case. Since ε

represents the misfit of the best-fitting model, the larger this value is, the lower the resolution.

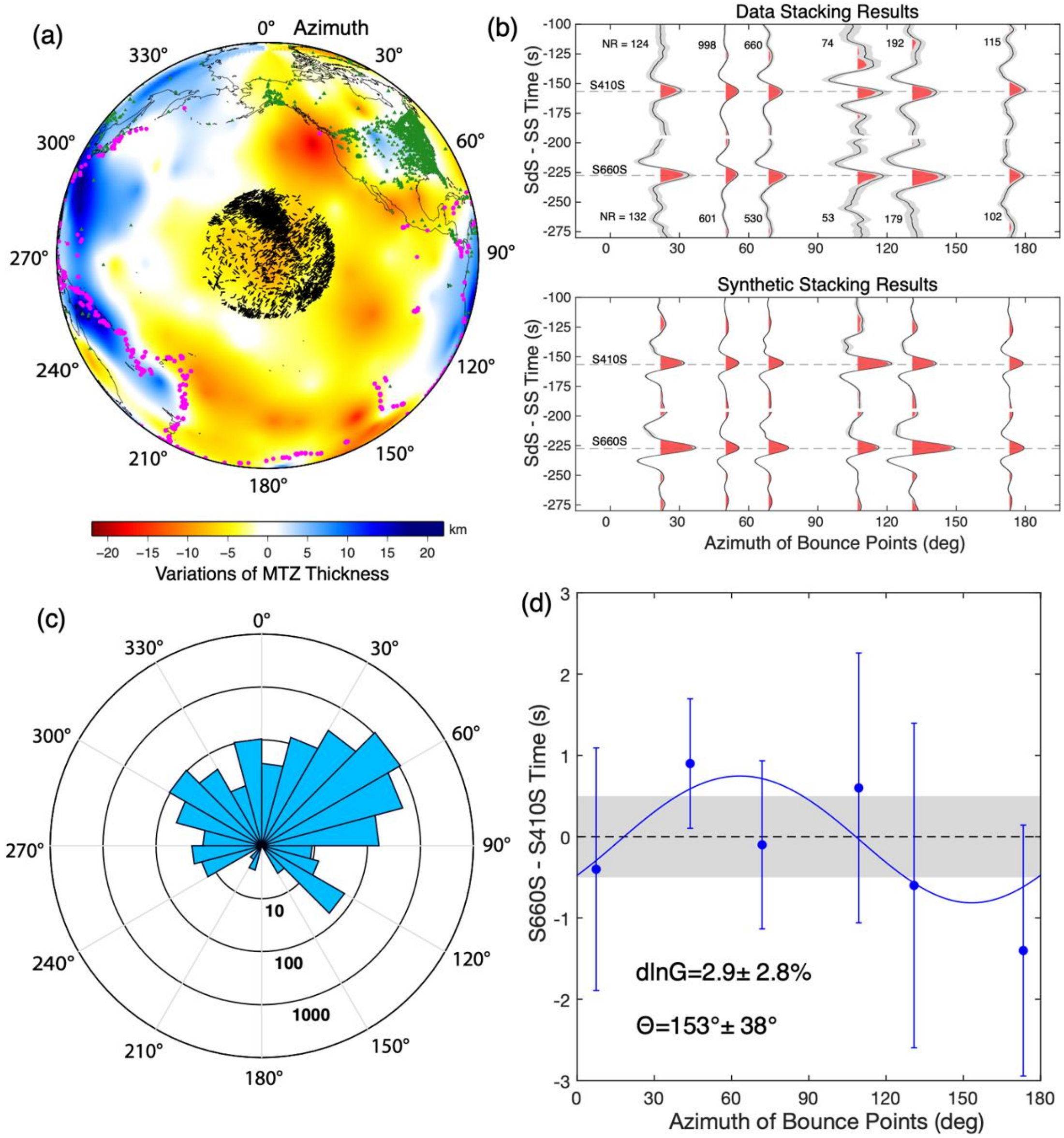

Figure 8. (a) The central Pacific bin of SS precursor data superimposed on the MTZ topography map. The MTZ thickness from Huang et al. (2019) is expressed as the variations with respect to the mean value 244.4 km. The black bars represent the SS bounce points and the azimuths of SS ray paths. The radius of the bin is 2000 km. The pink circles denote the earthquakes and the green triangles represent the stations. (b) The azimuthal stacking results of the data (top) and synthetics (bottom) in the central Pacific bin. The number of records (NR) of each azimuthal bin is labelled beside the waveform. The dashed lines highlight the average SdS travel times. (c) Rose diagram showing the azimuthal coverage of SS bounce points in log scale. (d) The S660S – S410S times and 2σ errors shown as a function of azimuth. The solid line is the best-fitting model. The dlnG and Θ values are the best-fitting strength of anisotropy and fast direction respectively. The dashed line is the average S660S-S410S time from the stacking of all azimuthal bins, and gray shaded box is the corresponding 2σ errors.

For the idealized geometry models, the resolutions of SdS travel times and amplitudes are shown in Figure 9. Generally, the detectability of anisotropy increases as the input anisotropy increases or the noise level decreases. Figure 9a illustrates that the S660S-S410S time can resolve 3% anisotropy with intermediate level of noise (SNR=7). Figure 9b suggests that the S660S-SS time has better resolution and can resolve 3% anisotropy even with higher levels of noise (SNR=4). However, our tests with shallow anisotropy demonstrates that S660S-SS time is also potentially affected by the upper mantle structure (Figure 4c), so it is not a unique indicator for MTZ anisotropy. The test also indicates that S410S and S660S amplitudes have lowered resolutions compared to the travel-time metrics. The S410S amplitude can only resolve 5% anisotropy with intermediate level of noise (Figure 9c), and the detectability of anisotropy with the S660S amplitude is always low even when noise is absent (Figure 9d). When using a more realistic geometry model, detectability is further degraded due to the lack of stations in the southern Pacific (Figure 10). However, despite the incomplete azimuthal coverage, our tests prove that the S660S-S410S time should present a detectable travel-time anomaly where there is 3% anisotropy in the central Pacific region (Figure 10a). The conclusion is that the central Pacific data have the potential to resolve 3% or greater anisotropy but the data failed to detect an anomaly of this magnitude, and as a result, the azimuthal anisotropy in this region is likely to be smaller than 3%.

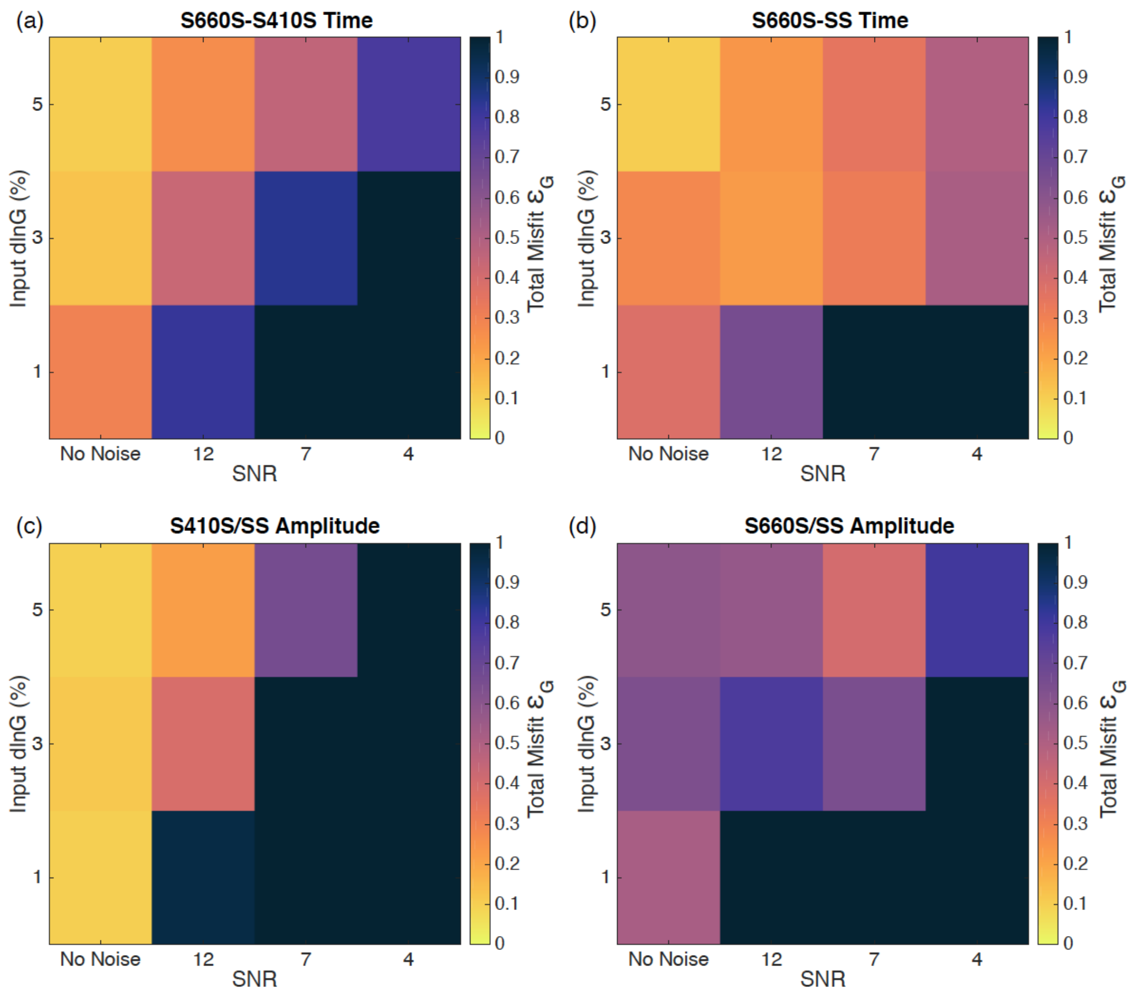

Figure 9. The resolution matrix for the central Pacific bin using an idealized source-receiver geometry. The dlnG resolution matrix for (a) S660S-S410S time, (b) S660S-SS time, (c) S410S/SS amplitude, and (d) S660S/SS amplitude. SNR=7 is the average noise level of our SS dataset. The total misfit ε_G of dlnG is inversely correlated with the resolution. When ε_G is greater than 1 (saturated in the plot), the model is considered as non-detectable.

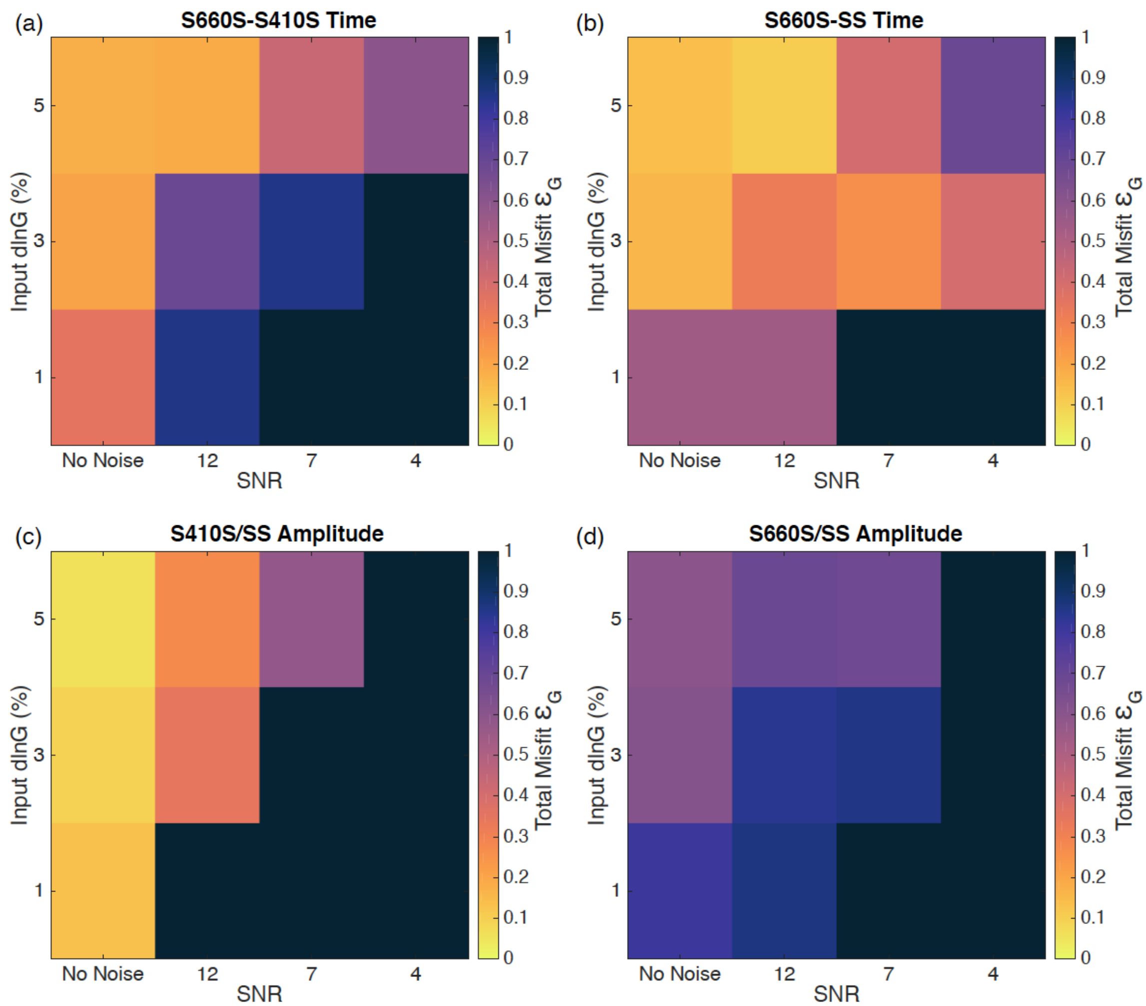

Figure 10. The same as Figure 9 but using a realistic source-receiver geometry. The dlnG resolution matrix for (a) S660S-S410S time, (b) S660S-SS time, (c) S410S/SS amplitude, and (d) S660S/SS amplitude.

3.3 Japan Subduction Zone

In Huang et al. (2019), we found evidence for ~3% MTZ anisotropy beneath the circum-Pacific subduction zones. However, the results were based on the stacking of multiple subduction zones, so there was ambiguity from which subduction zone originated the signal, or if it was ubiquitous amongst all subduction zones. Due to the relatively high density of data, we identified the Honshu subduction zone near Japan as a study region to uniquely determine the character of MTZ anisotropy. Honshu subduction zone is located in a region where the MTZ is thickened primarily due to the cold slab (e.g., Helffrich, 2000; Figure 11a). The tomography models also suggest that the Japan slab is stagnant above the 660-km discontinuity beneath eastern China and Korea (e.g., Fukao and Obayashi, 2013). We chose this region to study the mantle flow associated with the stagnant slab, and it is the best-sampled subduction zone in our SS dataset. However, the azimuthal coverage is relatively poor, with only four usable azimuthal bins for stacking and especially lacking the data with east-west orientations (Figure 11c). The data and synthetic stacking results are shown in Figure 11b. Despite limited data coverage, the S410S and S660S are recovered from stacking in all these four bins, noting that the S410S in 90 degrees bin (NR=2) is very noisy. We inverted the strength of anisotropy and fast direction from the S660S-S410S time (Figure 11d). The strength of anisotropy (dlnG=4.5±9.5%) is not significantly above zero due to the large uncertainties of travel-time measurement in 90° bin. The fast direction (Θ=87°±50°) is trench-perpendicular and shows relatively smaller uncertainties compared to dlnG. The fast direction is consistent with our observations in Huang et al. (2019), which suggests that the structure beneath Japan is representative of the structure found in the circum-Pacific subduction zones.

Following the Central Pacific study region methodology, we ran a similar resolution test for Japan subduction zone using both idealized and realistic source and receiver geometries (Figure 3). The resolution of the idealized geometry model is very similar to that of the central Pacific region although the bin size is smaller. However, the realistic geometry model using the actual azimuthal coverage of Japan displays poorer detectability in Figure 12. The SS precursors generally require tens of data points to obtain a stable stacking which is not the case here. Figure 12a illustrates that the S660S-S410S time can only resolve 5% anisotropy when noise level is very low (SNR=12) which is hardly observed in real data. Surprisingly, Figure 12b reveals that the resolution of fast directions is relatively higher, and S660S-S410S time can reconstruct the input fast direction of 3% anisotropy even when noise level is high (SNR=4). This suggests that SS precursors can still recover the input fast directions even if they cannot resolve the strength of anisotropy. This also indicates that the trench-perpendicular fast direction in Japan subduction zone is robust, thus can be used to infer mantle flow directions in the

MTZ. The S660S-SS time has slightly better resolution (Figure 12c), whereas the S410S amplitude has similar resolution to S660S-S410S time (Figure 12d).

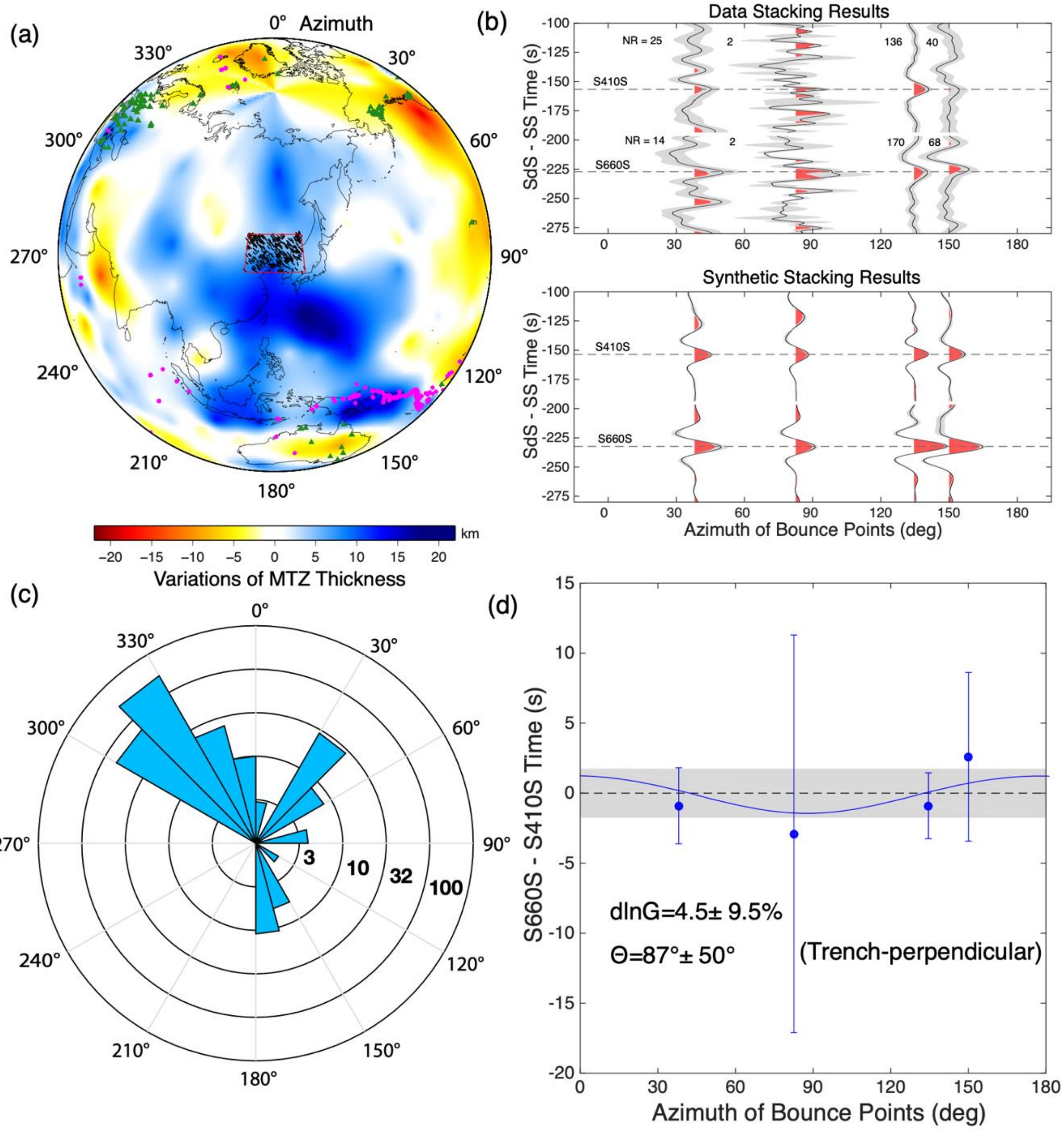

Figure 11. (a) The SS precursor data in Japan subduction zone superimposed on the MTZ topography map. The legends are the same as Figure 8. The study region is highlighted by the red box, and the size is 1500 km × 1000 km. (b) The azimuthal stacking results of the data (top) and synthetics (bottom) in Japan subduction zone. The number of records (NR) of each azimuthal bin is labelled beside the waveforms. The dashed lines highlight the average SdS travel times. (c) The rose diagram showing the azimuthal coverage of SS bounce points in log scale. (d) The S660S – S410S times and 2σ errors shown as a function of azimuths. The best-fitting fast direction is trench-perpendicular. The dashed line is the average S660S-S410S time from the stacking of all azimuthal bins, and gray shaded box is the corresponding 2σ

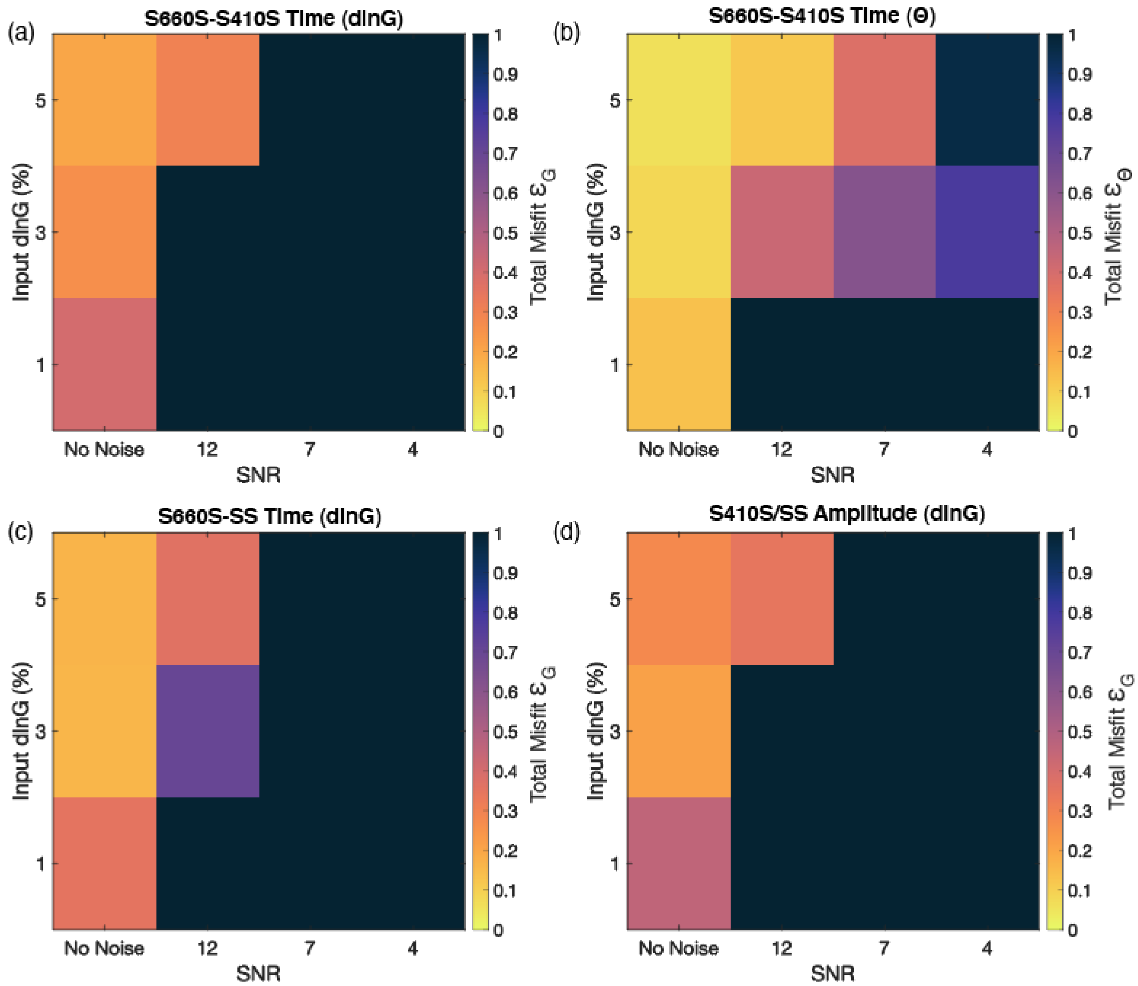

438

439 **Figure 12**. The resolution matrix for Japan subduction zone using a realistic source-receiver

440 geometry. The (a) dlnG and (b) Θ resolution matrix for S660S-S410S time. The dlnG resolution

441 matrix for (c) S660S-SS time and (d) S410S/SS amplitude.

442

443

444

445

446

447

448

449

450

4. Discussion

4.1 Proof of concept: the resolution and limitation of SS precursors

Currently, the two major tools to constrain deep mantle anisotropy are shear wave splitting and higher mode surface waves. However, the shear wave splitting method has limited vertical resolution to distinguish the origin depths of the anisotropy structures, and surface waves have low horizontal resolution (~6500 km in the MTZ from Visser et al, 2008, Yuan and Beghein, 2018) and cannot detect small-scale anisotropy such as the structures near subduction zones. We have demonstrated that stacks of the SS precursors have sensitivity to azimuthal anisotropy in the upper mantle and MTZ through 3-D synthetic modeling. The travel-times of SS precursors can resolve $\geq$3% azimuthal anisotropy in the MTZ with intermediate level of noise (SNR=7). The amplitudes of SS precursors shed light on the anisotropy change across a seismic discontinuity such as 410-km discontinuity (Saki et al., 2018). Due to the effect of stacking, the uncertainties of SdS amplitudes are often larger than travel-time measurements so they can only detect $\geq$5% azimuthal anisotropy in the MTZ. However, we can apply this method to a shallower upper mantle discontinuity with stronger anisotropy such as the lithosphere-asthenosphere boundary (LAB) or mid-lithosphere discontinuity (MLD) where the polarity change of the amplitudes can take place (e.g., Rychert et al., 2014; Wirth and Long, 2014).

Sufficient azimuthal coverage is key to successfully applying SS precursors to anisotropy studies. This method requires at least 4 to 5 different azimuths with NR>100 in each azimuthal bin to obtain a robust estimate of strength and fast direction of anisotropy. However, the lack of azimuthal coverage is common in our SS dataset, and we only identify four suitable candidate locations: (1) the northwestern Pacific, (2) the central Pacific, (3) the central Atlantic, and (4) Greenland (Huang et al., 2019). This is primarily due to the uneven distributions of large earthquakes concentrated near plate boundaries and dense stations mostly in North America (e.g., USArray). This means that although the western Pacific subduction zones have large numbers of records sampling the region, azimuthal coverage is actually quite limited. The data could be augmented by future ocean bottom seismometers (OBS) deployed across the Pacific Ocean (e.g., Kawakatsu et al., 2009).

A second challenge presented by this approach is the determination of the depth and thickness of the anisotropic layer. Our tests show that the SS precursors cannot resolve multiple sub-layers of anisotropy structures in the target depth range. For example, the SS precursors cannot distinguish whether MTZ anisotropy is located in the upper or lower MTZ, or the whole MTZ. Thus, in our modeling and data analysis, we only assume uniform anisotropy across the whole MTZ, which may underestimate the strength of anisotropy if it is only localized in a sub-layer. The final challenge is that we focus only on the SH waves to constrain azimuthal anisotropy, but SV waves can also provide useful information about anisotropy, via the splitting of the SS phase and its precursors (e.g., Wolfe & Silver, 1998). Despite these limitations, SS precursors can serve as a new method to constrain seismic anisotropy in the upper and mid-mantle, especially beneath oceanic regions where seismic stations are underpopulated for shear wave splitting measurements.

4.2 Interpretation of mantle flow in the transition zone

The central Pacific region reveals a non-detection of MTZ anisotropy near the Hawaiian hot spot. Few shear wave splitting studies have reported evidence for MTZ anisotropy in this region, either due to the interference of strong lithosphere and asthenosphere anisotropy (e.g. Collins et al., 2012) or simply lack of data. Therefore, we compare our results to three higher mode surface wave models at 500-km depth: YB13SVani (Yuan and Beghein, 2013), SL2016SvA (Schaeffer et al., 2016), and 3D2017_09Sv (Debayle et al., 2016). These three models only show 0.5–1.0% azimuthal anisotropy near Hawaiian hot spot. Ideally, the SS precursors can only detect 1% azimuthal anisotropy with very clean data (SNR > 12, Figure 9). In this case, the strength of MTZ anisotropy beneath Hawaiian hot spot is likely below our resolution. This suggests the mantle flow associated with the Hawaiian plume does not produce significant MTZ azimuthal anisotropy (Figure 13).

We find that the fast direction of MTZ anisotropy is trench-perpendicular (parallel to the Pacific plate motion direction) beneath the Japan subduction zone. The strength of anisotropy is less constrained compared to the fast direction because inversion of fast direction only requires azimuthal coverage in the fast and slow directions. The mantle flow direction can be inferred from the fast direction of azimuthal anisotropy. Our results are consistent with previous observations using source-side shear wave splitting measurements of deep earthquakes (e.g., Lynner and Long, 2015; Nowacki et al., 2015). Lynner and Long (2015) found evidence for azimuthal anisotropy originating from the MTZ and uppermost lower mantle beneath Japan, and the fast splitting direction is also trench-perpendicular. The higher mode surface wave model (Yuan and Beghein, 2018) shows trench-perpendicular fast direction as well at 450 km depth beneath Japan. The consistency among these three different methods combined with our 3-D synthetic modeling suggest that trench-perpendicular is a definitive feature of the MTZ beneath the Japan subduction zone. However, the fast splitting directions in the MTZ display a heterogeneous pattern across different subduction zones around the Pacific Ocean. Beneath Tonga subduction zone, the dominant fast direction is trench-parallel (Foley and Long, 2011; Mohiuddin et al., 2015); whereas the Sumatra and South America subduction zones show both trench-parallel and trench-perpendicular fast directions (Nowacki et al, 2015; Di Leo et al., 2012; Lynner and Long, 2015). Our previous study (Huang et al., 2019) combined all the data in the circum-Pacific subduction zones for stacking and concluded that trench-perpendicular fast direction is the most coherent pattern, however our data could be biased by Japan and South America where the data coverage is densest. The variability of fast directions also suggests heterogeneous flow patterns associated with different subducting slabs (penetrating or stagnant) in the mid-mantle.

The observed trench-perpendicular fast direction of MTZ anisotropy could be attributed either to the SPO of subducting slab, or the LPO of wadsleyite. Geodynamic modeling suggests that the strain induced LPO under a dislocation creep regime can better fit the global tomography model than SPO in the mid-mantle (Ferreira et al., 2019; Sturgeon et al., 2019). Therefore, we assume that LPO of wadsleyite is the primarily contributor to the MTZ anisotropy beneath the Japan subduction zone. This interpretation of mantle flow direction from the fast direction of mantle anisotropy requires the experimental data of wadsleyite's dominant slip systems (Sharp et al., 1994; Thurel et al., 2003; Demouchy et al, 2011; Kawazoe et al, 2013; Ohuchi et al., 2014). Kawazoe et al. (2013) reported that the dominant slip system of wadsleyite is [001] (010), therefore the mantle flow direction is perpendicular to the fast polarization direction of shear wave, which is the same as B-type olivine (e.g., Jung and Karato, 2001). Under the assumption of a [001] (010) slip system for wadsleyite, the seismic trench-perpendicular fast direction then infers trench-parallel flow near the stagnant Japan slab in the MTZ (Figure 13). The inferred flow also agrees with the trench-parallel flow directions in the sub-slab MTZ predicted by 3-D geodynamic modeling (Faccenda, 2014). Our previous study (Huang et al., 2019) reported that trench-parallel fast direction is dominant in the upper mantle beneath the slab, which is also consistent with trench-parallel flow assuming A-type olivine fabric (e.g., Karato et al., 2008). The trench-parallel flow around slabs is consistent with the toroidal flow induced by trench migration (Faccenda and Capitanio, 2012). Consequently, our results suggest the mantle flow direction remains consistently trench-parallel throughout the entire sub-slab upper mantle and transition zone in Japan (Figure 13). Alternatively, the flow direction in the transition zone can rotate by 90 degrees and become trench-perpendicular if we assume the dominant slip system of wadsleyite is [100] (0kl) (Demouchy et al., 2011). Other complexities such as the water and iron content in the MTZ (e.g. Zhang et al., 2018), mineral recrystallization through phase changes (e.g. Karato, 1988), and SPO of slabs would alter our interpretations.

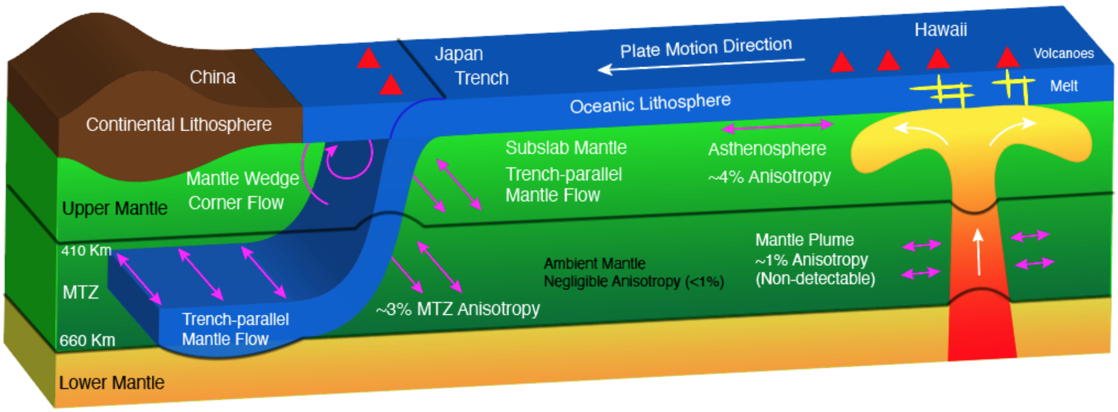

Figure 13. A schematic diagram depicting the mantle flow patterns in the upper mantle and transition zone observed from SS precursors. The pink arrows denote the inferred mantle flow direction from azimuthal anisotropy assuming A-type olivine in the upper mantle and [001] (010) slip system of wadsleyite in the MTZ (Kawazoe et al., 2013). On the left, the trench-parallel flow consistently exists in the sub-slab upper mantle and MTZ beneath Japan subduction zone (Huang et al., 2019). The trench-perpendicular fast direction near the stagnant slab is interpreted as trench-parallel flow in the MTZ as well. The mantle wedge is likely dominated by the trench-perpendicular corner flow which is not observed in our study. On the right, the Hawaiian mantle plume can only produce very weak azimuthal anisotropy (~1%) which is not detectable from SS precursors. The asthenosphere beneath Hawaii show strong azimuthal anisotropy (~4%) with a fast direction parallel to the plate motion direction (Huang et al., 2019). The azimuthal anisotropy is negligible (<1%) in the ambient mantle.

5. Conclusions

We have investigated the sensitivity of SS precursors to azimuthal anisotropy using 3-D synthetics computed from SPECFEM3D_GLOBE. We tested the following factors that affect the sensitivity of SS precursors: the depth of anisotropy, size and strength of anisotropy, source and receiver geometry, and noise level. We demonstrate that the SS precursors can distinguish between anisotropy in the upper mantle versus the MTZ via the azimuthal variations of SdS amplitudes and travel-times. The source and receiver geometry and azimuthal coverage both play key roles in constraining the strength of anisotropy and fast direction. When data coverage is sufficient (i.e., NR>100 in each azimuthal bin), the SS precursors can resolve ≥3% azimuthal anisotropy in the MTZ with average level of noise (SNR=7). In case of biased or limited azimuthal coverage (e.g., Japan), the fast direction can still be inverted from S660S-S410S time even if the strength of anisotropy is poorly constrained.

We searched for evidence for mantle flow associated with mantle plume or subducting slab in the MTZ beneath the central Pacific region and Japan subduction zone. In Japan subduction zone, we find evidence for trench-perpendicular fast direction (Θ=87°±50°) in the MTZ, which is consistent with previous shear-wave splitting and surface wave measurements. We attribute this MTZ anisotropy to the LPO of wadsleyite such that the trench-perpendicular fast direction in Japan is interpreted as trench-parallel mantle flow based on the dominant slip system of wadsleyite. We infer that the mantle flow direction beneath Japan is likely to remain consistently trench-parallel throughout the entire sub-slab upper mantle and transition zone. In the central Pacific region, the resolution test suggests that our data can resolve 3% anisotropy, but no anisotropy is detected. The MTZ anisotropy is probably << 3% beneath central Pacific, which is consistent with ~1% anisotropy from the surface wave models, and therefore below the resolution of SS precursors. This suggests that the vertical flow caused by the mantle plume beneath Hawaiian hotspot cannot produce strong azimuthal anisotropy in the MTZ.

Acknowledgements

The SS dataset was downloaded from Incorporated Research Institutions for Seismology, Data Management Center (IRIS DMC). The SS dataset and MTZ topography model are available at http://hdl.handle.net/1903/21819 (DOI: https://doi.org/10.13016/3ecr-1hsu). We also thank the developers of SPECFEM3D for distributing the codes freely online. QH and NS were supported by the National Science Foundation (NSF) under grant NO. EAR-1447041. CB was supported by NSF under grant NO. EAR-1446978. LW is the recipient of a Discovery Early Career Research Award (project number DE170100329) funded by the Australian Government and supported by NSF under grant NO. EAR-1661985 and EAR-1853662. RM was supported by NSF EAR Postdoctoral Fellowship 1806412.

References

Anderson, D. L. (1962). LOVE WAVE DISPERSION IN HETEROGENEOUS ANISOTROPIC MEDIA. *Geophysics*, *27*(4), 427–541. http://doi.org/https://doi.org/10.1190/1.1439042

Bai, L., Zhang, Y., & Ritsema, J. (2012). An analysis of SS precursors using spectral-element method seismograms. *Geophysical Journal International*, *188*(1), 293–300. http://doi.org/10.1111/j.1365-246X.2011.05256.x

Bass, J. D., & Kanzaki, M. (1990). Elasticity of a majorite- pyrope solid solution. *Geophysical Research Letters*, *17*(11), 1989–1992. http://doi.org/10.1029/GL017i011p01989

Bassin, C., Laske, G., & Masters, G. (2000). The current limits of resolution for surface wave tomography in North America. *EOS Trans. AGU. 81 : Fall Meet. Suppl., Abstract*.

Becker, T. W., Chevrot, S., Pelkum, V. S., & Blackman, D. K. (2006). Statistical properties of seismic anisotropy predicted by upper mantle geodynamic models. *Journal of Geophysical Research: Solid Earth*, *111*(B8), 12253. http://doi.org/10.1029/2005JB004095

Becker, T. W., Lebedev, S., & Long, M. D. (2012). On the relationship between azimuthal anisotropy from shear wave splitting and surface wave tomography. *Journal of Geophysical Research: Solid Earth*, *117*(B1), B01306. http://doi.org/10.1029/2011JB008705

Beghein, C., Resovsky, J., & van der Hilst, R. D. (2008). The signal of mantle anisotropy in the coupling of normal modes. *Geophysical Journal International*, *175*(3), 1209–1234. http://doi.org/10.1111/j.1365-246X.2008.03970.x

Bercovici, D., & Karato, S.-I. (2003). Whole-mantle convection and the transition-zone water filter. *Nature*, *425*(6953), 39–44. http://doi.org/10.1038/nature01918

Bina, C. R., & Helffrich, G. (1994). Phase transition Clapeyron slopes and transition zone seismic discontinuity topography. *Journal of Geophysical Research: Solid Earth*, *99*(B8), 15853–15860. http://doi.org/10.1029/94JB00462

Chang, S.-J., Ferreira, A. M. G., Ritsema, J., van Heijst, H. J., & Woodhouse, J. H. (2015). Joint inversion for global isotropic and radially anisotropic mantle structure including crustal thickness perturbations. *Journal of Geophysical Research: Solid Earth*, *120*(6), 4278–4300. http://doi.org/10.1002/2014JB011824

Chen, W. P., & Brudzinski, M. R. (2003). Seismic anisotropy in the mantle transition zone beneath Fiji- Tonga. *Geophysical Research Letters*, *30*(13). http://doi.org/10.1029/2002GL016330

Collins, J. A., Wolfe, C. J., & Laske, G. (2012). Shear wave splitting at the Hawaiian hot spot from the PLUME land and ocean bottom seismometer deployments. *Geochemistry, Geophysics, Geosystems*, *13*(2), n/a–n/a. http://doi.org/10.1029/2011GC003881

Crampin, S. (1984). An introduction to wave propagation in anisotropic media. *Geophysical Journal International*, *76*(1), 17–28. http://doi.org/10.1111/j.1365-246X.1984.tb05018.x

Debayle, E., Dubuffet, F., & Durand, S. (2016). An automatically updated S-wave model of the upper mantle and the depth extent of azimuthal anisotropy. *Geophysical Research Letters*, *43*(2), 674–682. http://doi.org/10.1002/2015GL067329

Demouchy, S., Mainprice, D., Tommasi, A., Couvy, H., Barou, F., Frost, D. J., & Cordier, P. (2011). Forsterite to wadsleyite phase transformation under shear stress and consequences for the Earth's mantle transition zone. *Physics of the Earth and Planetary Interiors*, *184*(1-2), 91–104. http://doi.org/10.1016/j.pepi.2010.11.001

Deuss, A., & Woodhouse, J. H. (2002). A systematic search for mantle discontinuities using SS- precursors. *Geophysical Research Letters*, *29*(8), 90–1–90–4. http://doi.org/10.1029/2002GL014768

Di Leo, J. F., Wookey, J., Hammond, J. O. S., Kendall, J. M., Kaneshima, S., Inoue, H., et al. (2012). Mantle flow in regions of complex tectonics: Insights from Indonesia. *Geochemistry, Geophysics, Geosystems*, *13*(12), 253. http://doi.org/10.1029/2012GC004417

Dziewonski, A. M., & Anderson, D. L. (1981). Preliminary reference Earth model. *Physics of the Earth and Planetary Interiors*, *25*(4), 297–356. http://doi.org/10.1016/0031-9201(81)90046-7

Efron, B., & Tibshirani, R. (1986). Bootstrap methods for standard errors, confidence intervals, and other measures of statistical accuracy. *Statistical Science*. http://doi.org/10.2307/2245500

Faccenda, M. (2014). Mid mantle seismic anisotropy around subduction zones. *Physics of the Earth and Planetary Interiors*, *227*, 1–19. http://doi.org/10.1016/j.pepi.2013.11.015

Faccenda, M., & Capitanio, F. A. (2012). Development of mantle seismic anisotropy during subduction- induced 3- D flow. *Geophysical Research Letters*, *39*(11), n/a–n/a. http://doi.org/10.1029/2012GL051988

Faccenda, M., Ferreira, A. M. G., Tisato, N., Bertelloni, C. L., Stixrude, L., & Pennacchioni, G. (2019). Extrinsic Elastic Anisotropy in a Compositionally Heterogeneous Earth's Mantle. *Journal of Geophysical Research: Solid Earth*, *124*(2), 1671–1687. http://doi.org/10.1029/2018JB016482

Ferreira, A. M. G., Faccenda, M., Sturgeon, W., Chang, S.-J., & Schardong, L. (2019). Ubiquitous lower-mantle anisotropy beneath subduction zones. *Nature Geoscience*, *12*(4), 301–306. http://doi.org/10.1038/s41561-019-0325-7

Flanagan, M. P., & Shearer, P. M. (1998). Global mapping of topography on transition zone velocity discontinuities by stacking SS precursors. *Journal of Geophysical Research: Solid Earth*, *103*(B2), 2673–2692. http://doi.org/10.1029/97JB03212

Foley, B. J., & Long, M. D. (2011). Upper and mid- mantle anisotropy beneath the Tonga slab. *Geophysical Research Letters*, *38*(2), L02303. http://doi.org/10.1029/2010GL046021

Fouch, M. J., & Fischer, K. M. (1996). Mantle anisotropy beneath northwest Pacific subduction zones. *Journal of Geophysical Research: Solid Earth*, *101*(B7), 15987–16002. http://doi.org/10.1029/96JB00881

French, S. W., & Romanowicz, B. A. (2014). Whole-mantle radially anisotropic shear velocity structure from spectral-element waveform tomography. *Geophysical Journal International*, *199*(3), 1303–1327. http://doi.org/10.1093/gji/ggu334

Friederich, W., & Dalkolmo, J. (1995). Complete synthetic seismograms for a spherically symmetric earth by a numerical computation of the Green's function in the frequency domain. *Geophysical Journal International*, *122*(2), 537–550. http://doi.org/10.1111/j.1365-246X.1995.tb07012.x

Fukao, Y., & Obayashi, M. (2013). Subducted slabs stagnant above, penetrating through, and trapped below the 660 km discontinuity. *Journal of Geophysical Research: Solid Earth*, *118*(11), 5920–5938. http://doi.org/10.1002/2013JB010466

Gu, Y. J., & Dziewonski, A. M. (2002). Global variability of transition zone thickness. *Journal of Geophysical Research: Solid Earth*, *107*(B7), ESE 2–1–ESE 2–17. http://doi.org/10.1029/2001JB000489

Gu, Y., Dziewonski, A. M., & Agee, C. B. (1998). Global de-correlation of the topography of transition zone discontinuities. *Earth and Planetary Science Letters*, *157*(1-2), 57–67. http://doi.org/10.1016/S0012-821X(98)00027-2

Hayes, G. P., Wald, D. J., & Johnson, R. L. (2012). Slab1.0: A three-dimensional model of global subduction zone geometries. *Journal of Geophysical Research: Solid Earth*, *117*(B1), B01302. http://doi.org/10.1029/2011JB008524

Helffrich, G. (2000). Topography of the transition zone seismic discontinuities. *Reviews of Geophysics*, *38*(1), 141–158. http://doi.org/10.1029/1999RG000060

Houser, C., Masters, G., Flanagan, M., & Shearer, P. (2008). Determination and analysis of long-wavelength transition zone structure using SS precursors. *Geophysical Journal International*, *174*(1), 178–194. http://doi.org/10.1111/j.1365-246X.2008.03719.x

Huang, Q., Schmerr, N., Waszek, L., & Beghein, C. (2019). Constraints on Seismic Anisotropy in the Mantle Transition Zone From Long- Period SS Precursors. *Journal of Geophysical Research: Solid Earth*, 618. http://doi.org/10.1029/2019JB017307

Ita, J., & Stixrude, L. (1992). Petrology, elasticity, and composition of the mantle transition zone. *Journal of Geophysical Research: Solid Earth*, *97*(B5), 6849–6866. http://doi.org/10.1029/92JB00068

Ito, E., & Takahashi, E. (1989). Postspinel transformations in the system Mg2SiO4- Fe2SiO4 and some geophysical implications. *Journal of Geophysical Research: Solid Earth*, *94*(B8), 10637–10646. http://doi.org/10.1029/JB094iB08p10637

Jung, H., & Karato, S.-I. (2001). Water-Induced Fabric Transitions in Olivine. *Science*, *293*(5534), 1460–1463. http://doi.org/10.1126/science.1062235

Karato, S. (1988). The Role of Recrystallization in the Preferred Orientation of Olivine. *Physics of the Earth and Planetary Interiors*, *51*(1-3), 107–122. http://doi.org/10.1016/0031-9201(88)90029-5

Karato, S.-I., Jung, H., Katayama, I., & Skemer, P. (2008). Geodynamic Significance of Seismic Anisotropy of the Upper Mantle: New Insights from Laboratory Studies. *Dx.Doi.org*, *36*(1), 59–95. http://doi.org/10.1146/annurev.earth.36.031207.124120

Katsura, T., & Ito, E. (1989). The system Mg2SiO4- Fe2SiO4 at high pressures and temperatures: Precise determination of stabilities of olivine, modified spinel, and spinel. *Journal of Geophysical Research: Solid Earth*, *94*(B11), 15663–15670. http://doi.org/10.1029/JB094iB11p15663

Kawakatsu, H., Kumar, P., Takei, Y., Shinohara, M., Kanazawa, T., Araki, E., & Suyehiro, K. (2009). Seismic Evidence for Sharp Lithosphere-Asthenosphere Boundaries of Oceanic Plates. *Science*, *324*(5926), 499–502. http://doi.org/10.1126/science.1169499

Kawazoe, T., Ohuchi, T., Nishihara, Y., Nishiyama, N., Fujino, K., & Irifune, T. (2013). Seismic anisotropy in the mantle transition zone induced by shear deformation of wadsleyite. *Physics of the Earth and Planetary Interiors*, *216*, 91–98. http://doi.org/10.1016/j.pepi.2012.12.005

Kiefer, B., Stixrude, L., & Wentzcovitch, R. M. (1997). Calculated elastic constants and anisotropy of Mg2SiO4 spinel at high pressure. *Geophysical Research Letters*, *24*(22), 2841–2844. http://doi.org/10.1029/97GL02975

Komatitsch, D., & Tromp, J. (2002a). Spectral-element simulations of global seismic wave propagation-II. Three-dimensional models, oceans, rotation and self-gravitation. *Geophysical Journal International*, *150*(1), 303–318. http://doi.org/10.1046/j.1365-246X.2002.01716.x

Komatitsch, D., & Tromp, J. (2002b). Spectral-element simulations of global seismic wave propagation—I. Validation. *Geophysical Journal International*, *149*(2), 390–412. http://doi.org/doi.org/10.1046/j.1365-246X.2002.01653.x

Koroni, M., & Trampert, J. (2016). The effect of topography of upper-mantle discontinuities on SS precursors. *Geophysical Journal International*, *204*(1), 667–681. http://doi.org/10.1093/gji/ggv471

Lawrence, J. F., & Shearer, P. M. (2008). Imaging mantle transition zone thickness with SdS-SS finite-frequency sensitivity kernels. *Geophysical Journal International*, *174*(1), 143–158. http://doi.org/10.1111/j.1365-246X.2007.03673.x

Li, J., Zheng, Y., Thomsen, L., Lapen, T. J., & Fang, X. (2018). Deep earthquakes in subducting slabs hosted in highly anisotropic rock fabric. *Nature Geoscience*, *11*(9), 696–700. http://doi.org/10.1038/s41561-018-0188-3

Li, L., Weidner, D. J., Brodholt, J., Alfè, D., & Price, G. D. (2006). Elasticity of Mg2SiO4 ringwoodite at mantle conditions. *Physics of the Earth and Planetary Interiors*, *157*(3-4), 181–187. http://doi.org/10.1016/j.pepi.2006.04.002

Long, M. D., & Van Der Hilst, R. D. (2005). Upper mantle anisotropy beneath Japan from shear wave splitting. *Physics of the Earth and Planetary Interiors*, *151*(3-4), 206–222. http://doi.org/10.1016/j.pepi.2005.03.003

Lynner, C., & Long, M. D. (2015). Heterogeneous seismic anisotropy in the transition zone and uppermost lower mantle: evidence from South America, Izu-Bonin and Japan. *Geophysical Journal International*, *201*(3), 1545–1552. http://doi.org/10.1093/gji/ggv099

Marone, F., & Romanowicz, B. (2007). The depth distribution of azimuthal anisotropy in the continental upper mantle. *Nature*, *447*(7141), 198–U4. http://doi.org/10.1038/nature05742

Mohiuddin, A., Long, M. D., & Lynner, C. (2015). Mid-mantle seismic anisotropy beneath southwestern Pacific subduction systems and implications for mid-mantle deformation. *Physics of the Earth and Planetary Interiors*, *245*, 1–14. http://doi.org/10.1016/j.pepi.2015.05.003

Mondal, P., & Long, M. D. (2020). Strong seismic anisotropy in the deep upper mantle beneath the Cascadia backarc: Constraints from probabilistic finite-frequency SKS splitting intensity tomography. *Earth and Planetary Science Letters*, *539*, 116172. http://doi.org/10.1016/j.epsl.2020.116172

Montagner, J. P. (2002). Upper mantle low anisotropy channels below the Pacific Plate. *Earth and Planetary Science Letters*, *202*(2), 263–274. http://doi.org/10.1016/S0012-821X(02)00791-4

Montagner, J.-P., & Nataf, H. C. (1986). A simple method for inverting the azimuthal anisotropy of surface waves. *Journal of Geophysical Research: Solid Earth*, *91*(B1), 511–520. http://doi.org/10.1029/JB091iB01p00511

Montagner, J.-P., Griot Pommera, D. A., & Lavé, J. (2000). How to relate body wave and surface wave anisotropy? *Journal of Geophysical Research: Solid Earth*, *105*(B8), 19015–19027. http://doi.org/10.1029/2000JB900015

Morgan, J. P., & Shearer, P. M. (1993). Seismic constraints on mantle flow and topography of the 660-km discontinuity: evidence for whole-mantle convection. *Nature*, *365*(6446), 506–511. http://doi.org/10.1038/365506a0

Moulik, P., & Ekström, G. (2014). An anisotropic shear velocity model of the Earth's mantle using normal modes, body waves, surface waves and long-period waveforms. *Geophysical Journal International*, *199*(3), 1713–1738. http://doi.org/10.1093/gji/ggu356

Nettles, M., & Dziewonski, A. M. (2008). Radially anisotropic shear velocity structure of the upper mantle globally and beneath North America. *Journal of Geophysical Research: Solid Earth*, *113*(B2), 219. http://doi.org/10.1029/2006JB004819

Nowacki, A., Kendall, J. M., Wookey, J., & Pemberton, A. (2015). Mid-mantle anisotropy in subduction zones and deep water transport. *Geochemistry, Geophysics, Geosystems*, *16*(3), 764–784. http://doi.org/10.1002/2014GC005667

Ohuchi, T., Fujino, K., Kawazoe, T., & Irifune, T. (2014). Crystallographic preferred orientation of wadsleyite and ringwoodite: Effects of phase transformation and water on seismic anisotropy in the mantle transition zone.

Earth and Planetary Science Letters, *397*, 133–144. http://doi.org/10.1016/j.epsl.2014.03.066

Pamato, M. G., Kurnosov, A., Boffa Ballaran, T., Frost, D. J., Ziberna, L., Giannini, M., et al. (2016). Single crystal elasticity of majoritic garnets: Stagnant slabs and thermal anomalies at the base of the transition zone. *Earth and Planetary Science Letters*, *451*, 114–124. http://doi.org/10.1016/j.epsl.2016.07.019

Peterson, J. R. (1993). Observations and modeling of seismic background noise. *Open-File Report*, (93-322). http://doi.org/10.3133/ofr93322

Ringwood, A. E. (1975). Composition and petrology of the earth's mantle. McGraw-Hill, New York.

Ritsema, J., Deuss, A., van Heijst, H. J., & Woodhouse, J. H. (2011). S40RTS: a degree-40 shear-velocity model for the mantle from new Rayleigh wave dispersion, teleseismic traveltime and normal-mode splitting function measurements. *Geophysical Journal International*, *184*(3), 1223–1236. http://doi.org/10.1111/j.1365-246X.2010.04884.x

Rychert, C. A., Harmon, N., & Schmerr, N. (2014). Synthetic waveform modelling of SS precursors from anisotropic upper-mantle discontinuities. *Geophysical Journal International*, *196*(3), 1694–1705. http://doi.org/10.1093/gji/ggt474

Rychert, C. A., Schmerr, N., & Harmon, N. (2012). The Pacific lithosphere-asthenosphere boundary: Seismic imaging and anisotropic constraints from SS waveforms. *Geochemistry, Geophysics, Geosystems*, *13*(9), 83. http://doi.org/10.1029/2012GC004194

Saki, M., Thomas, C., Merkel, S., & Wookey, J. (2018). Detecting seismic anisotropy above the 410 km discontinuity using reflection coefficients of underside reflections. *Physics of the Earth and Planetary Interiors*, *274*, 170–183. http://doi.org/10.1016/j.pepi.2017.12.001

Sang, L., & Bass, J. D. (2014). Single-crystal elasticity of diopside to 14 GPa by Brillouin scattering. *Physics of the Earth and Planetary Interiors*, *228*, 75–79. http://doi.org/10.1016/j.pepi.2013.12.011

Sawamoto, H., Weidner, D. J., Sasaki, S., & Kumazawa, M. (1984). Single-crystal elastic properties of the modified spinal (beta) phase of magnesium orthosilicate. *Science*, *224*(4650), 749–752. http://doi.org/10.1126/science.224.4650.749

Schaeffer, A. J., Lebedev, S., & Becker, T. W. (2016). Azimuthal seismic anisotropy in the Earth's upper mantle and the thickness of tectonic plates. *Geophysical Journal International*, *207*(2), 901–933. http://doi.org/10.1093/gji/ggw309

Schmerr, N., & Garnero, E. (2006). Investigation of upper mantle discontinuity structure beneath the central Pacific using SS precursors. *Journal of Geophysical Research: Solid Earth*, *111*(B8), B08305. http://doi.org/10.1029/2005JB004197

Schmerr, N., Garnero, E., & McNamara, A. (2010). Deep mantle plumes and convective upwelling beneath the Pacific Ocean. *Earth and Planetary Science Letters*, *294*(1-2), 143–151. http://doi.org/10.1016/j.epsl.2010.03.014

Sharp, T. G., Bussod, G. Y. A., & Katsura, T. (1994). Microstructures in β-Mg1.8Fe0.2SiO4 experimentally deformed at transition-zone conditions. *Physics of the Earth and Planetary Interiors*, *86*(1-3), 69–83. http://doi.org/10.1016/0031-9201(94)05062-7

Silver, P. G., & Chan, W. W. (1988). Implications for continental structure and evolution from seismic anisotropy. *Nature*, *335*(6185), 34–39. http://doi.org/10.1038/335034a0

Sinogeikin, S. V., Bass, J. D., & Katsura, T. (2003). Single-crystal elasticity of ringwoodite to high pressures and high temperatures: implications for 520 km seismic discontinuity. *Physics of the Earth and Planetary Interiors*, *136*(1-2), 41–66. http://doi.org/10.1016/S0031-9201(03)00022-0

Sinogeikin, S. V., Katsura, T., & Bass, J. D. (1998). Sound velocities and elastic properties of Fe- bearing wadsleyite and ringwoodite. *Journal of Geophysical Research: Solid Earth*, *103*(B9), 20819–20825. http://doi.org/10.1029/98JB01819

Stixrude, L. (1997). Structure and sharpness of phase transitions and mantle discontinuities. *Journal of Geophysical Research: Solid Earth*, *102*(B7), 14835–14852. http://doi.org/10.1029/97JB00550

Sturgeon, W., Ferreira, A. M. G., Faccenda, M., Chang, S.-J., & Schardong, L. (2019). On the Origin of Radial Anisotropy Near Subducted Slabs in the Midmantle. *Geochemistry, Geophysics, Geosystems*, *464*(11), 10. http://doi.org/10.1029/2019GC008462

Thomas, C., & Billen, M. I. (2009). Mantle transition zone structure along a profile in the SW Pacific: Thermal and compositional variations. *Geophysical Journal International*, *176*(1), 113–125. http://doi.org/10.1111/j.1365-246X.2008.03934.x

Thurel, E., Cordier, P., Frost, D., & Karato, S. I. (2003). Plastic deformation of wadsleyite: II. High-pressure deformation in shear. *Physics and Chemistry of Minerals*, *30*(5), 267–270. http://doi.org/10.1007/s00269-003-0313-7

Tommasi, A., Mainprice, D., Cordier, P., Thoraval, C., & Couvy, H. (2004). Strain-induced seismic anisotropy of wadsleyite polycrystals and flow patterns in the mantle transition zone. *Journal of Geophysical Research: Solid Earth*, *109*(B12). http://doi.org/10.1029/2004JB003158

Tong, C., Gudmundsson, O., & Kennett, B. L. N. (1994). Shear wave splitting in refracted waves returned from the upper mantle transition zone beneath northern Australia. *Journal of Geophysical Research: Solid Earth*, *99*(B8), 15783–15797. http://doi.org/10.1029/94JB00460

Trampert, J., & van Heijst, H. J. (2002). Global Azimuthal Anisotropy in the Transition Zone. *Science*, *296*(5571), 1297–1299. http://doi.org/10.1126/science.1070264

Visser, K., Trampert, J., & Kennett, B. L. N. (2008). Global anisotropic phase velocity maps for higher mode Love and Rayleigh waves. *Geophysical Journal International*, *172*(3), 1016–1032. http://doi.org/10.1111/j.1365-246X.2007.03685.x

Waszek, L., Schmerr, N. C., & Ballmer, M. D. (2018). Global observations of reflectors in the mid-mantle with implications for mantle structure and

dynamics. *Nature Communications*, *9*(1), 385. http://doi.org/10.1038/s41467-017-02709-4
Weidner, D. J., Sawamoto, H., Sasaki, S., & Kumazawa, M. (1984). Single-crystal elastic properties of the spinel phase of Mg2SiO4. *Journal of Geophysical Research: Solid Earth*, *89*(B9), 7852–7860. http://doi.org/10.1029/JB089iB09p07852
Wirth, E. A., & Long, M. D. (2014). A contrast in anisotropy across mid-lithospheric discontinuities beneath the central United States—A relic of craton formation. *Geology*, *42*(10), 851–854. http://doi.org/10.1130/G35804.1
Wolfe, C. J., & Silver, P. G. (1998). Seismic anisotropy of oceanic upper mantle: Shear wave splitting methodologies and observations. *Journal of Geophysical Research: Solid Earth*, *103*(B1), 749–771. http://doi.org/10.1029/97JB02023
Yu, C., Day, E. A., de Hoop, M. V., Campillo, M., & van der Hilst, R. D. (2017). Mapping Mantle Transition Zone Discontinuities Beneath the Central Pacific With Array Processing of SS Precursors. *Journal of Geophysical Research: Solid Earth*, *122*(12), 10,364–10,378. http://doi.org/10.1002/2017JB014327
Yuan, K., & Beghein, C. (2013). Seismic anisotropy changes across upper mantle phase transitions. *Earth and Planetary Science Letters*, *374*, 132–144. http://doi.org/10.1016/j.epsl.2013.05.031
Yuan, K., & Beghein, C. (2014). Three- dimensional variations in Love and Rayleigh wave azimuthal anisotropy for the upper 800 km of the mantle. *Journal of Geophysical Research: Solid Earth*, *119*(4), 3232–3255. http://doi.org/10.1002/2013JB010853
Yuan, K., & Beghein, C. (2018). A Bayesian method to quantify azimuthal anisotropy model uncertainties: application to global azimuthal anisotropy in the upper mantle and transition zone. *Geophysical Journal International*, *213*(1), 603–622. http://doi.org/10.1093/gji/ggy004
Zha, C. S., Duffy, T. S., Mao, H. K., Downs, R. T., Hemley, R. J., & Weidner, D. J. (1997). Single-crystal elasticity of β-Mg2SiO4 to the pressure of the 410 km seismic discontinuity in the Earth's mantle. *Earth and Planetary Science Letters*, *147*(1-4), E9–E15. http://doi.org/10.1016/S0012-821X(97)00010-1
Zhang, J. S., Bass, J. D., & Schmandt, B. (2018). The Elastic Anisotropy Change Near the 410- km Discontinuity: Predictions From Single- Crystal Elasticity Measurements of Olivine and Wadsleyite. *Journal of Geophysical Research: Solid Earth*, *123*(4), 2674–2684. http://doi.org/10.1002/2017JB015339
Zhao, L., & Chevrot, S. (2003). SS- wave sensitivity to upper mantle structure: Implications for the mapping of transition zone discontinuity topographies. *Geophysical Research Letters*, *30*(11), 1590. http://doi.org/10.1029/2003GL017223